

Mapping the kinetic Sunyaev-Zel'dovich effect toward MACS J0717.5+3745 with NIKA

R. Adam^{1*}, I. Bartalucci², G.W. Pratt², P. Ade³, P. André², M. Arnaud², A. Beelen⁴, A. Benoît⁵, A. Bideaud³, N. Billot⁶, H. Bourdin⁷, O. Bourrion⁸, M. Calvo⁵, A. Catalano⁸, G. Coiffard⁹, B. Comis⁸, A. D'Addabbo^{5,10}, M. De Petris¹⁰, F.-X. Désert¹¹, J. Démocles², S. Doyle³, E. Egami¹², C. Ferrari¹, J. Goupy⁵, C. Kramer⁶, G. Lagache¹³, S. Leclercq⁹, J.-F. Macías-Pérez⁸, S. Maurogordato¹, P. Mauskopf^{3,14}, F. Mayet⁸, A. Monfardini⁵, T. Mroczkowski¹⁵, F. Pajot⁴, E. Pascale³, L. Perotto⁸, G. Pisano³, E. Pointecouteau^{16,17}, N. Ponthieu¹¹, V. Revéret², A. Ritacco⁸, L. Rodriguez², C. Romero⁹, F. Ruppin⁸, K. Schuster⁹, A. Sievers⁶, S. Triqueneaux⁵, C. Tucker³, M. Zemcov^{18,19}, and R. Zylka⁹

¹ Laboratoire Lagrange, Université Côte d'Azur, Observatoire de la Côte d'Azur, CNRS, Blvd de l'Observatoire, CS 34229, 06304 Nice cedex 4, France

² Laboratoire AIM, CEA/IRFU, CNRS/INSU, Université Paris Diderot, CEA-Saclay, 91191 Gif-Sur-Yvette, France

³ Astronomy Instrumentation Group, University of Cardiff, UK

⁴ Institut d'Astrophysique Spatiale (IAS), CNRS and Université Paris Sud, Orsay, France

⁵ Institut Néel, CNRS and Université Grenoble Alpes, France

⁶ Institut de RadioAstronomie Millimétrique (IRAM), Granada, Spain

⁷ Dipartimento di Fisica, Università degli Studi di Roma 'Tor Vergata', via della Ricerca Scientifica, 1, I-00133 Roma, Italy

⁸ Laboratoire de Physique Subatomique et de Cosmologie, Université Grenoble Alpes, CNRS/IN2P3, 53, avenue des Martyrs, Grenoble, France

⁹ Institut de RadioAstronomie Millimétrique (IRAM), Grenoble, France

¹⁰ Dipartimento di Fisica, Sapienza Università di Roma, Piazzale Aldo Moro 5, I-00185 Roma, Italy

¹¹ Institut de Planétologie et d'Astrophysique de Grenoble (IPAG), CNRS and Université Grenoble Alpes, France

¹² Steward Observatory, University of Arizona, 933 North Cherry Avenue, Tucson, AZ 85721, USA

¹³ Aix Marseille Université, CNRS, LAM (Laboratoire d'Astrophysique de Marseille) UMR 7326, 13388, Marseille, France

¹⁴ School of Earth and Space Exploration and Department of Physics, Arizona State University, Tempe, AZ 85287

¹⁵ U.S. Naval Research Laboratory, 4555 Overlook Ave SW, Washington, D.C. 20375, USA

¹⁶ Université de Toulouse, UPS-OMP, Institut de Recherche en Astrophysique et Planétologie (IRAP), Toulouse, France

¹⁷ CNRS, IRAP, 9 Av. colonel Roche, BP 44346, F-31028 Toulouse cedex 4, France

¹⁸ California Institute of Technology, 1200 E. California Blvd., Pasadena, CA 91125, USA

¹⁹ Jet Propulsion Laboratory, 4800 Oak Grove Drive, Pasadena, CA 91109, USA

Received June 6, 2016 / Accepted –

Abstract

Measuring the gas velocity distribution in galaxy clusters provides a precious insight into the physics of mergers, from which large scale structures form in the Universe. The Sunyaev-Zel'dovich (SZ) effect is a way to do so, but its observation is challenging both in term of sensitivity requirement and control of systematic effects, including the removal of contaminants. In this paper we report resolved observations, at 150 and 260 GHz, of the SZ effect toward the triple merger MACS J0717.5+3745 ($z = 0.55$), using data obtained with the kinetic inductance detector camera, NIKA, at the IRAM 30m telescope. Assuming that the SZ signal is the sum of a thermal (tSZ) and a kinetic (kSZ) component and by combining the two NIKA bands, we extract for the first time a map of the kSZ signal in a cluster. The kSZ emission is dominated by a dipolar structure that peaks at -5.1 and $+3.4\sigma$, corresponding to two sub-clusters moving respectively away and toward us and coincident with the cold dense X-ray core and a hot region undergoing a violent merging event. We investigate the effect of possible contamination and systematic effects with a special care given to radio and sub-millimeter point sources. Among the sources that we detect with NIKA, we find one which is likely to be a high redshift lensed sub-millimeter galaxy. We then model the gas electronic density and line of sight velocity of MACS J0717.5+3745 by four sub-clusters. By combining NIKA to X-ray data, we fit this model to constrain the gas line of sight velocity of each component, and we also derive, for the first time, a velocity map from kSZ data. Our results are consistent with previous work and provide an improvement of the angular resolution of the measurement by a factor of ~ 3 , allowing in particular for the mapping of the kSZ signal.

Key words. Techniques: high angular resolution – Galaxies: clusters: individual: MACS J0717.5+3745; intracluster medium

1. Introduction



The assembly of massive clusters of galaxies represents the last step of the hierarchical formation of structures in the Universe. Galaxy clusters arise from smooth accretion of surrounding ma-

terial, but also from the merging of sub-clusters and groups, at the intersection of filaments in the cosmic web (see Kravtsov & Borgani 2012, for a review). These mergers are not only useful large scales–astrophysical laboratories (e.g., Clowe et al. 2006), but they are important from a cosmological point of view (e.g., Voit 2005). The physical processes involved in mergers signifi-

* Corresponding author: Rémi Adam, remi.adam@oca.eu

cantly affect the cluster observables via the distribution of dark matter, the physics of the intracluster plasma, and the distribution of galaxies (e.g., Ferrari et al. 2005; Maurogordato et al. 2011), i.e., all the components of the clusters. These observables are in turn essential to infer the masses of clusters when used as a cosmological probe (see Allen et al. 2011, for a review). In this context, measuring the velocity distribution of merging systems provides insights of the cluster physics, such as shocks in the intracluster medium (ICM), the kinematics of the mergers, the hydrodynamical interactions between cluster cores and less dense shock heated regions and the relation between the baryonic matter and the dark matter. In addition, as mergers are driven by the collapse of structures under the action of gravity, the peculiar velocity distribution of galaxy clusters is related to the underlying cosmology. Therefore, such velocity measurements provide a complementary cosmological probe to constrain structure formation (Bhattacharya & Kosowsky 2007) and the understanding of the properties of the velocity field is a subject of active research (e.g., using numerical simulations, Hahn et al. 2015). Clusters peculiar velocities are particularly sensitive to the redshift evolution of dark energy (Hernández-Monteagudo et al. 2006; Bhattacharya & Kosowsky 2008; Ma & Zhao 2014) and can be used to distinguish it from modified gravity models (Kosowsky & Bhattacharya 2009).

Measuring the peculiar velocity of galaxy clusters is a difficult task, in particular when looking at objects beyond the local Universe. Indeed, classical methods, that are based on redshift surveys, allow to reconstruct the internal galaxy kinematics of clusters but require an independent distance measurement to subtract the Hubble flow at the objects positions in order to measure their absolute peculiar velocities (for example, the Tully-Fisher relation, Tully & Fisher 1977), and are therefore limited to small redshifts as the errors scale with distance. The Sunyaev-Zel'dovich effect (SZ, Birkinshaw 1999; Carlstrom et al. 2002; Kitayama 2014), on the other hand, provides a way to probe the ICM gas bounded in clusters without suffering from the cosmological dimming of the signal surface brightness. Observation is therefore independent of redshift as long as the angular resolution of the observations is sufficient to resolve the source. We can distinguish between the thermal SZ effect (tSZ, Sunyaev & Zeldovich 1972), for which the cosmic microwave background (CMB) photons are spectrally distorted by the electronic thermal pressure of the ICM, from the kinetic SZ effect (kSZ, Sunyaev & Zeldovich 1980), arising from the CMB Doppler shift induced by the bulk motion of the electrons of the cluster electrons. While the tSZ effect is related to the integrated pressure along the line of sight and can be used as a mass proxy in various cosmological studies (see, e.g., Planck Collaboration et al. 2015c; Bleem et al. 2015; Hasselfield et al. 2013), the kSZ effect is sensitive to the integrated line of sight electronic density and the absolute gas velocity with respect to the CMB reference frame. The kSZ signal is subdominant with respect to the tSZ unless the gas velocity reaches a few tenths of a percent of the speed of light (1000 km/s). In addition, the kSZ spectral dependency is the same as the CMB, so that it can only be separated spatially from the latter. The direct observation of the kSZ signal within clusters therefore requires both high sensitivity and high angular resolution observations (Haehnelt & Tegmark 1996), which makes its particularly challenging to detect in individual clusters. Several attempts to measure the kSZ effect have been performed toward individual clusters (e.g. Holzapfel et al. 1997; Benson et al. 2003; Adam et al. 2015; Sayers et al. 2015) and on statistical samples (e.g. Kashlinsky et al. 2008; Planck Collaboration et al. 2014b). While Kashlinsky et al. (2008) claimed for the de-

tection of a large amplitude Hubble flow, their results have been disputed in the literature (see Atrio-Barandela 2013), and the first clear kSZ detection was obtained only recently by Hand et al. (2012) using the mean pairwise momentum of a large sample of clusters (see also Soergel et al. 2016, for a recent result). The kSZ effect was also used to detect unbound gas at large scales from the cross correlation between kSZ fluctuations and central galaxies radial peculiar velocities (Planck Collaboration et al. 2015a).

The cluster of galaxies MACS J0717.5+3745 at $z = 0.55$ is a striking example of a merging system and constitutes a primary choice-target for measuring the kSZ effect, as discussed below. It was discovered in the MASSive Cluster Survey (MACS, Ebeling et al. 2001; Edge et al. 2003) and since then, a wealth of multi-wavelength data have been obtained toward this cluster. A detailed review of the previous analysis of MACS J0717.5+3745 can be found in Mroczkowski et al. (2012) and Sayers et al. (2013), and we summarize essential features here. The cluster is located at the end of a filamentary structure (Ebeling et al. 2004; Kartaltepe et al. 2008; Jauzac et al. 2012; Medezinski et al. 2013) and appears to be an extremely disturbed system. It is made of four optically-identified main sub-clusters (labeled from A to D, following Ma et al. 2009), which coincide with peaks in the observed strong lensing surface mass distribution (Zitrin et al. 2009, 2011; Limousin et al. 2012; Medezinski et al. 2013; Johnson et al. 2014; Kawamata et al. 2015; Zitrin et al. 2015; Diego et al. 2015; Limousin et al. 2015). The X-ray emitting gas is very disturbed (Ebeling et al. 2007; Ma et al. 2009; Mroczkowski et al. 2012). It shows a dense core in the direction of sub-cluster B, a disturbed structure between C and D, and sub-cluster A is almost invisible in X-ray, suggesting that it corresponds to a group that has already passed through the main cluster, being stripped from its gas. The X-ray spectroscopic temperature (Ma et al. 2009; Mroczkowski et al. 2012; Sayers et al. 2013) is very high between C and D ($\gtrsim 20$ keV), in agreement with the two groups being undergoing a violent merging event. Sub-cluster B, on the other hand, is much colder (~ 10 keV), and is likely to be still relatively intact, in a premerging state. Edge et al. (2003) discovered the presence of powerful radio emission around group C and D, indicating the presence of non-thermal support in this region (see also van Weeren et al. 2009; Bonafede et al. 2009; Pandey-Pommier et al. 2013, for more recent studies). MACS J0717.5+3745 was also observed using 30 GHz interferometric SZ data by the Sunyaev-Zel'dovich Array (SZA), indicating that the cluster was a hot and massive system (LaRoque et al. 2003). Mroczkowski et al. (2012) reported high angular resolution (effective beam FWHM of 13 arcsec) SZ observations at 90 GHz using MUSTANG (The Multiplexed SQUID/TES Array at Ninety GHz) at the Green Bank Telescope (GBT). The data revealed small scales structures in the pressure distribution between C and D and emission toward B, in agreement with the merger scenario. The velocity distribution of MACS J0717.5+3745 was first studied using optical spectroscopy (Ma et al. 2009), showing that the galaxy groups have exceptionally large relative line of sight velocities, providing a more detailed picture of the merger kinematics ($v_z^A = 278^{+295}_{-339}$ km/s, $v_z^B = 3238^{+252}_{-242}$ km/s, $v_z^C = -733^{+486}_{-478}$ km/s, $v_z^D = 831^{+843}_{-800}$ km/s). Using Bolocam SZ data at 140 and 268 GHz, Mroczkowski et al. (2012) reported the first indication of the presence of kSZ signal in MACS J0717.5+3745 from the difference between their two bands, finding a velocity toward sub-cluster B and C consistent with optical measurement. Sayers et al. (2013) then reported the first significant detection of the kSZ signal in a single cluster, MACS J0717.5+3745, after

collecting additional data with Bolocam and refining the former analysis. As the Bolocam beams are larger than the target sub-clusters (58 and 31 arcsec FWHM at 140 and 268 GHz, respectively), the limited angular resolution of these data is one of the restraining factor of the kSZ detection.

In this paper we report deep high angular resolution observations (20 arcsec) of MACS J0717.5+3745 at 150 and 260 GHz, obtained at the Institut de Radio Astronomie Millimétrique (IRAM) 30-m telescope using the New IRAM KID Arrays (NIKA, a kinetic inductance detectors camera, Monfardini et al. 2011; Calvo et al. 2013; Adam et al. 2014; Catalano et al. 2014) camera. The resolved nature of the observations allows us for a robust treatment of the contaminating astrophysical signal and the data are used to produce a map of the kSZ signal toward the cluster. Combining X-ray spectroscopic temperature measurements to NIKA, we also fit a parametric model to constrain the gas line of sight velocity distribution.

The paper is organized as follows. In section 2, we present the SZ observations of MACS J0717.5+3745. The removal of the astrophysical contamination is presented and discussed in section 3. In section 4, we detail the X-ray data reduction. In section 5, we present the mapping of the kSZ effect in MACS J0717.5+3745 and we use our data together with X-ray temperatures to constrain the gas line of sight velocity in section 6. Throughout this paper we assume a flat Λ CDM cosmology according to the latest *Planck* results (Planck Collaboration et al. 2015b) with $H_0 = 67.8 \text{ km s}^{-1} \text{ Mpc}^{-1}$, $\Omega_M = 0.308$, and $\Omega_\Lambda = 0.692$.

2. Sunyaev-Zel'dovich observations and data reduction

2.1. The Sunyaev-Zel'dovich effect

The SZ effect consists in the spectral distortion of the CMB due to the inverse Compton scattering of CMB photons on energetic electrons in galaxy clusters. Only the thermal and the kinetic SZ effects have been observed so far (induced by a thermal electron population and the bulk motion of electrons with respect to the CMB, respectively), but in principle the SZ effect can also arise from the CMB interaction onto more exotic electron populations, such as ones originating from dark matter annihilation (Colafrancesco 2004) or ultra-relativistic electrons accelerated in radio lobes (Colafrancesco 2008). Nevertheless, these other contributions are expected to be small and, in this paper, we assume that only the tSZ and the kSZ effects contribute the SZ signal.

The tSZ effect follows the characteristic frequency dependence given by (Birkinshaw 1999)

$$f(x, T_e) = \frac{x^4 e^x}{(e^x - 1)^2} \left(4 - x \coth\left(\frac{x}{2}\right) \right) (1 + \delta_{\text{tSZ}}(x, T_e)), \quad (1)$$

where $x = \frac{hv}{k_B T_{\text{CMB}}}$ is the dimensionless frequency, with v the observing frequency, h the Planck's constant, k_B the Boltzmann's constant, and the CMB temperature $T_{\text{CMB}} = 2.725 \text{ K}$ (Fixsen 2009). The term $\delta_{\text{tSZ}}(x, T_e)$ corresponds to relativistic corrections, which depends on the observing frequency and the electron temperature T_e , and which we compute using the work of Itoh & Nozawa (2003). These corrections are valid at a level of $\lesssim 5\%$ up to 50 keV within the NIKA bands.

The spectral dependence of the kSZ effect follows that of the CMB, in the non relativistic regime. It is given by (Birkinshaw

1999)

$$g(x, v_z, T_e) = \frac{x^4 e^x}{(e^x - 1)^2} (1 + \delta_{\text{kSZ}}(x, v_z, T_e)), \quad (2)$$

where v_z is the gas line of sight velocity¹ and δ_{kSZ} the relativistic corrections, which depend on the observing frequency, T_e and v_z . We use the analytical formula provided by Nozawa et al. (2006) to compute relativistic corrections, which we expect to be more accurate than $\sim 10\%$ up to 30 keV in the NIKA bands. The velocity dependence on these corrections is negligible because v_z is always much smaller than the speed of light.

The observed change of specific intensity, ΔI_ν , with respect to the CMB, I_0 , is then given by

$$\frac{\Delta I_\nu}{I_0} = f(\nu, T_e) y_{\text{tSZ}} + g(\nu, T_e, v_z) y_{\text{kSZ}}, \quad (3)$$

where the amplitude of the tSZ and the kSZ signal are given by

$$y_{\text{tSZ}} = \frac{\sigma_T}{m_e c^2} \int P_e dl \equiv \frac{k_B T_e}{m_e c^2} \tau \quad (4)$$

and

$$y_{\text{kSZ}} = \sigma_T \int \frac{-v_z}{c} n_e dl \equiv \frac{-v_z}{c} \tau, \quad (5)$$

respectively. The parameter σ_T is the Thomson cross section, m_e the electron rest mass, c the speed of light, and n_e the electronic gas density. The kSZ and tSZ amplitudes can also be expressed using the optical depth, τ , as given in equations 4 (assuming constant temperature along the line of sight) and 5 (assuming constant velocity along the line of sight). As the ICM is a dilute medium, we assume the ideal gas law to hold and express the electronic pressure as $P_e = n_e k_B T_e$. The functions $f(\nu, T_e)$ and $g(\nu, T_e, v_z)$ are integrated in the NIKA bands, and the values are listed in table 1 for a few electronic gas temperature values, accounting for the NIKA beam solid angle to express them in terms of Jy/beam. While the tSZ signal is always negative at 150 GHz and positive at 260 GHz, the kSZ signal can be either positive or negative, depending on the sign of the velocity along the line of sight, but its sign is the same at both NIKA frequencies. The kSZ maximum corresponds to the null of the tSZ signal and is located around 217 GHz if relativistic effects are negligible.

2.2. NIKA observations and data reduction

MACS J0717.5+3745 was observed for 7.26 hours on target in February 2014 and 5.85 hours in January and February 2015. Most of the observations took place under good conditions, with a mean zenith opacity of 0.116 at 260 GHz and 0.085 at 150 GHz, and a stable atmosphere. The pointing center was (R.A., Dec.)_{J2000} = (07:17:32.3, +37:44:47) for the 2014 data set and (R.A., Dec.)_{J2000} = (07:17:32.3, +37:45:10) for 2015. The scanning strategy was the same as the one employed for other NIKA clusters as detailed in (Adam et al. 2015, 2016). Similarly, the detailed calibration procedure can be found in Adam et al. (2014, 2015). It results in a root mean square pointing error of $\lesssim 3$ arcsec, the absolute calibration uncertainties are 7% at 150 GHz and 12% at 260 GHz, and the gaussian beams FWHM were measured to be 18.2 and 12.0 arcsec at 150 and 260 GHz, respectively.

¹ The line of sight velocity is positive for a cluster receding from the observer.

Table 1. Spectral conversion coefficients. The units are Jy/beam per unit of y_{tSZ} and Jy/beam per unit of y_{kSZ} for $I_0 f(\nu)$ and $I_0 g(\nu)$, respectively. The uncertainty on the NIKA bandpasses is about 2% (see Adam et al. 2014, for more details) and are included in the overall calibration budget (see section 2.2). The coefficients given here account for the atmospheric absorption based on the Pardo et al. (2002) model for 2mm precipitable water vapor above the telescope, which slightly changes the effective NIKA bandpasses.

T_e (keV)	$I_0 f(260 \text{ GHz})$	$I_0 f(150 \text{ GHz})$	$I_0 g(260 \text{ GHz})$	$I_0 g(150 \text{ GHz})$
1	3.76	-11.63	7.47	12.40
5	3.31	-11.34	7.30	12.03
10	2.83	-11.00	7.11	11.62
15	2.43	-10.71	6.94	11.24
20	2.06	-10.38	6.81	10.90
25	1.76	-10.17	6.75	10.58

The data were reduced similarly and independently for the two bands, as described in Adam et al. (2015). The removal of the correlated noise across the arrays, mainly the atmospheric contribution but also the correlated electronic noise, leads to the filtering of the astrophysical signal at scales that are larger than the NIKA field of view (~ 2 arcmin). The resulting transfer function was computed using simulations. It is close to unity at small scales and vanishes smoothly at scales larger than the field of view. Apart from the beam smoothing, the transfer function was checked to be the same at 150 and 260 GHz, which allows for the direct combining of the two maps. The beam efficiency correction as a function of elevation was optimized for extended emission (Greve et al. 1998), which can lead to up to $\sim 10\%$ loss in the flux of point sources for very high or very low elevations. However, most of the data were taken between elevations of 35 and 62 degrees, with a mean of 49 degrees, such that we expect this bias to be less than a few percent and we neglect it.

The instrumental noise and the atmospheric noise residuals are estimated as detailed in Adam et al. (2016). In brief, we compute noise maps from the difference between two equivalent subsamples. These maps are normalized by the integration time spent per pixel in order to have a homogeneous noise in the observed sky patch. The homogeneous noise is then used to compute its power spectra (using the POKER software, Ponthieu et al. 2011), which is well described by a white component plus a pixel-pixel correlated contribution. This model finally allows to simulate noise maps accounting for the noise inhomogeneity, and to compute the full noise covariance matrix from noise Monte Carlo realization. We also estimate the cross correlation between the 150 and 260 GHz noise using the cross spectra of the difference maps. We observe a small correlation due to the atmospheric noise residuals, which we expect because NIKA observes the sky simultaneously at 150 and 260 GHz. The corresponding correlated noise between the two bands corresponds to 0.22% of the variance at 260 GHz, and 1.25% of the 150 GHz one. However, this is negligible with respect to the cross correlation induced by the cosmic infrared background (CIB) contamination (see section 3.1) and we do not account for it.

2.3. NIKA raw maps

The NIKA maps are shown in figure 1. They have been smoothed with a Gaussian filter to have the same effective resolution of 22 arcsec FWHM. Due to the integration time spent per sky pixels, the noise is relatively constant within a radius of 1.5 arcmin around the map centers and increases radially toward the edges. At the 22 arcsec effective resolution, the noise root mean squared at the center of the field is $97 \mu\text{Jy}/\text{beam}$ at 150 GHz and $226 \mu\text{Jy}/\text{beam}$ at 260 GHz, accounting for instrumental noise, residual atmospheric noise but also the astrophysical noise as

discussed in section 3.1. The noise root mean square on the flux of a point source located near the center is 0.14 mJy at 150 GHz and 0.58 mJy at 260 GHz. The positions of the four regions that we consider, A, B, C and D, are also shown in figure 1. Various coordinates have been provided in the literature, obtained for example by fitting dark matter profiles on strong lensing data (e.g., Limousin et al. 2012, 2015). Since we are interested in the gas distribution rather than the dark matter, we use the cored best fit model coordinates of Limousin et al. (2015) as a starting point but we slightly adjust them to match the peak distribution of the X-ray Chandra wavelet smoothed map, taking as a prior for the gas distribution (see top right panel of figure 3). These coordinates (see table 2) are, however, consistent with strong lensing within the dispersion obtained from the different models by Limousin et al. (2015). Unless otherwise stated, they are used only for display purpose in this paper and the choice of these regions has no impact on the overall results that we present.

Table 2. Definition of the location of the four sub-clusters in MACS J0717.5+3745. These regions are defined using Limousin et al. (2015) strong lensing fit and the Chandra X-ray surface brightness (see also figure 6).

Sub-cluster	R.A.	Dec.
A	+07:17:25.0	+37:45:54.6
B	+07:17:31.3	+37:45:30.3
C	+07:17:35.8	+37:45:01.0
D	+07:17:33.0	+37:44:15.0

The 150 GHz map shows the presence of diffuse negative signal associated to the SZ effect. It is dominated by the tSZ emission at this frequency, but the kSZ emission is also significant (see section 5). The signal is non zero, but very small in the direction of sub-cluster A, in agreement with its expected low gas content as discussed in section 1. The brightness in the direction of all other sub-clusters is significant with a peak between regions B and C, reaching -18.4σ . However, we do not observe peaked emission in the direction of each group, but rather a diffuse signal which does not allow to clearly identify the sub-clusters using this map. We also report the detection of a foreground radio galaxy on the southeast with respect to the cluster (see section 3.2).

At 260 GHz, we observe diffuse positive emission around regions C reaching up to 4.3σ at the peak, but the surface brightness in region B is negative, with a peak at -3.7σ . We also observe a deficit of surface brightness slightly above region D but much weaker. The signal to noise is insufficient to detect the signal in region A at 260 GHz. We also detect three point sources

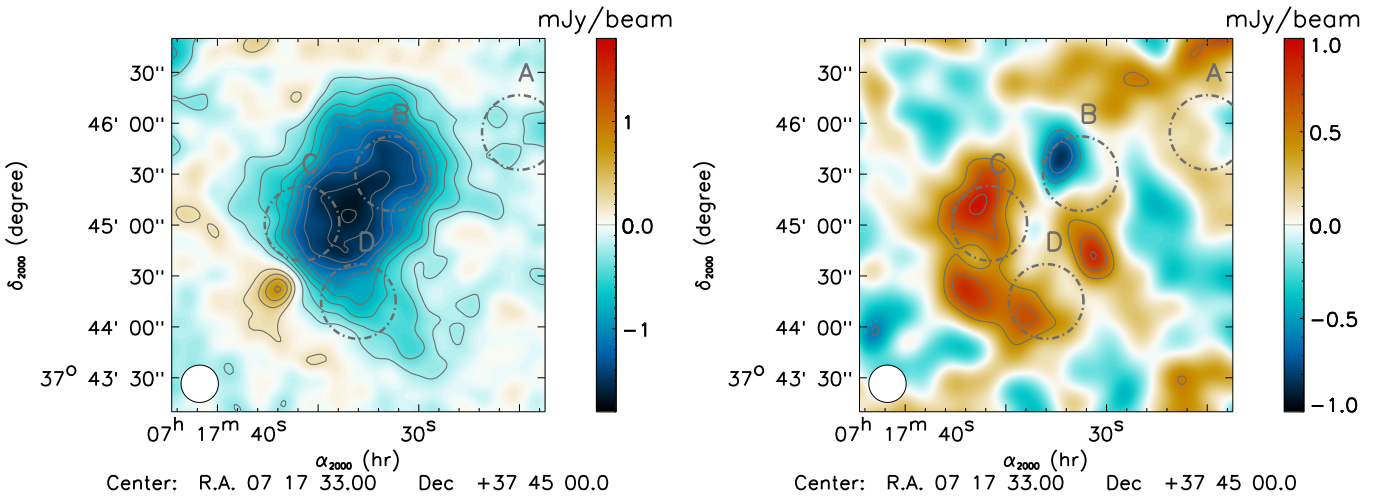


Figure 1. NIKA maps of MACS J0717.5+3745 at 150 GHz (left) and 260 GHz (right). The gray contours show the significance in unit of standard deviation. They are multiple of 2σ at 150 GHz and 1σ at 260 GHz, starting at $\pm 2\sigma$. Both maps have been smoothed to have an effective resolution of 22 arcsec FWHM, as represented by the white circle on the bottom left corner of the maps. The regions defined in table 2 are shown as white dashed circles.

 We directly on the map: one is coincident with the foreground galaxy seen at 150 GHz; a source is located on the south of region D; and the last one is located northwest with respect to region D. We note that this last source is also visible at 150 GHz when applying a Mexican hat filter on the map. Due to the relatively high astrophysical contamination ~~already~~ observed in the 260 GHz map, its detailed interpretation requires the removal and the treatment of the point sources as it will be discussed in section 3. Nevertheless, ~~we can already notice~~ that we observe an excess of signal around region C with respect to the 150 GHz ~~pure~~ tSZ expectation, and negative signal in region B ~~by opposition~~ to the positive tSZ emission expected at this frequency. While the former could be attributed to another astrophysical signal, it is not the case for the latter which we will interpret as a kSZ signature in section 5.

3. Astrophysical contamination of the Sunyaev-Zel'dovich signal

In addition to the SZ emission from the cluster itself, we expect galactic, extragalactic, and cluster associated astrophysical signal to contaminate our data. This section describes how such contaminants are taken into account in the present paper.

3.1. Diffuse galactic emission and cosmological background

We reproduce the  detailed in Adam et al. (2016) in order to check that the CMB and the galactic emission (we consider synchrotron, free-free and thermal dust) are negligible in the case of MACS J0717.5+3745 NIKA data. The CIB was also considered in Adam et al. (2016). Despite being the largest diffuse astrophysical contribution, it was shown to be negligible. The data we present here, however, are about seven times deeper, such that the CIB is no longer negligible and requires more careful investigation as we discuss below.

We consider the clustering of dusty star forming galaxies, the shot noise from dusty star forming galaxies and the shot noise from radio sources. The clustering term from radio sources is negligible (Hall et al. 2010). The clustering of dusty  forming galaxies is computed using the CIB power spectrum measured by Planck Collaboration et al. (2014a) at 143 and 217

GHz. It is modeled by a one halo term and a two halo term and extrapolated to the NIKA frequencies. The shot noise is due to unresolved sources below the detection threshold of NIKA. For dusty star forming galaxies, it is computed using the model from Béthermin et al. (2012), and we use the model of Tucci et al. (2011) for radio sources. We account for the beam smoothing and the large scale filtering implied by the NIKA processing. At the angular scales considered from the NIKA data, the shot noise dominates over the clustering by a factor of about five, and the shot noise from radio sources is negligible compared to the one from dusty star forming galaxies at both NIKA frequencies. Using the results of Béthermin et al. (2013), we assume that the CIB is completely correlated between the two NIKA bands. At our effective angular resolution of 22 arcsec, we find that the noise root mean squared of the CIB is $47 \mu\text{Jy}/\text{beam}$ at 150 GHz and $130 \mu\text{Jy}/\text{beam}$ at 260 GHz. This boosts the noise in our maps by 22.1% and 14.8% at 260 and 150 GHz, respectively, and induces a noise correlation between the two bands. The uncertainty on the CIB model that we use is expected to be about 20%. This translates to 7% and 5% uncertainty on the overall noise estimate at 260 and 150 GHz, respectively. In addition to the uncertainties in the model itself, we note that our CIB estimate is likely to be slightly overestimated in the field of MACS J0717.5+3745, because we expect dimming due to the gravitational lensing by the cluster mass (Zemcov et al. 2013).

3.2. Radio sources

First, we consider the diffuse radio emission associated with the cluster. We extrapolate the NVSS (NRAO VLA Sky Survey, at an angular resolution of 45 arcsec, see Condon et al. 1998) and FIRST (Faint Images of the Radio Sky at Twenty Centimeters, at an angular resolution of 5.4 arcsec, see Becker et al. 1995) maps assuming a spectral index of -1.25 following van Weeren et al. (2009) and Bonafede et al. (2009). We find that the radio emission is negligible in both cases within the NIKA bands. Moreover, this constitutes an upper limit on the radio contamination because we expect the radio spectra to be steeper at higher frequencies due to energy loss of the synchrotron emitting electrons (Scheuer & Williams 1968). Therefore, we do not correct for the extrapolated signal and neglect its contribution.

Table 3. Coordinates of the seven compact radio sources identified in the NIKA field.

Label	R.A.	Dec.
HT	+07:17:35.4	+37:45:08 ^(a)
B	+07:17:40.9	+37:43:17 ^(a)
F	+07:17:37.2	+37:44:21 ^(a)
C1	+07:17:38.4	+37:46:50 ^(b)
C2	+07:17:36.4	+37:44:03 ^(c)
C3	+07:17:23.5	+37:45:31 ^(b)
C4	+07:17:36.3	+37:44:44 ^(c)

Notes. ^(a) Bonafede et al. (2009). ^(b) FIRST catalog, <http://sundog.stsci.edu/cgi-bin/searchfirst>, (see Condon et al. 1998). ^(c) Pandey-Pommier et al. (2013).

In addition to the diffuse radio emission, a total of seven compact radio sources are identified in the NIKA field from the literature (see results by Condon et al. 1998; LaRoque et al. 2003; Coble et al. 2007; Bonafede et al. 2009; van Weeren et al. 2009; Mroczkowski et al. 2012; Pandey-Pommier et al. 2013), at lower frequencies. Their coordinates are listed in table 3. One of them, a foreground radio galaxy at $z = 0.1546$ (van Weeren et al. 2009), is significantly detected by NIKA at 150 and 260 GHz (source F, southeast of sub-cluster C, also detected in the Chandra X-ray image). Following Adam et al. (2016), we assume the radio SED to follow a power law in order to model the contamination in the NIKA bands. Since we know that the field around MACS J0717.5+3745 is relatively crowded, and to avoid source confusion, we only use photometric data from which the observations are sensitive to scales smaller than 30 arcsec: FIRST, VLA (Very Large Array), GMRT (Giant Metrewave Radio Telescope), OVRO/BIMA (Owens Valley Radio Observatory / Berkeley Illinois Maryland Association) and MUSTANG/GBT. We also extract the flux of the sources from the NIKA maps as detailed in Adam et al. (2016), except for sources HT and C4, which are located near the peak of the SZ emission. The available fluxes used to constrain the SED model, including the NIKA ones, are listed in table 4. In the case of source F, the spectrum is poorly described by our model over the full frequency coverage. Instead, the SED presents two distinct spectral indices at low (< 2 GHz) and high (> 10 GHz) frequencies. This is likely due to significant free-free emission at high frequencies in addition to the synchrotron at low frequencies, but might also indicate biases in the measurement of the flux (obtained with different instrument) because of the source extension and location, near the radio relic at low frequencies. Therefore, we assume that the power law model is valid at high frequency only and consider data at $\nu > 10$ GHz. Despite indication for steepening, the other sources are correctly described by a power law. In the case of sources C1, C2, C3 and C4, however, the limited number of available data suggests to interpret the model prediction with caution. In addition, we emphasize that the NIKA photometry might be contaminated by sub-millimeter sources, as discussed in section 3.3, and possibly also by SZ emission. The results flux prediction in the NIKA bands are listed in table 4 and are used as discussed in the following. All predicted fluxes are compatible with the one measured directly with NIKA. The source model, i.e. the 150 and 260 GHz best fit fluxes of table 4, is given in figure 2, including sub-millimeter sources, as discussed in section 3.3.

3.3. Sub-millimeter point sources

As already mentioned in section 2.3, sub-millimeter sources significantly contaminate our data, even at 150 GHz. We use the method detailed in Adam et al. (2016) in order to subtract their contribution. To do so, in addition to the NIKA data themselves, we use the SPIRE (Spectral and Photometric Imaging REceiver, Griffin et al. 2010) catalog produced by Sayers et al. (2013) to clean their Bolocam images. Eleven sources are identified in the 4 arcmin \times 4 arcmin around the cluster and we report their fluxes in table 5. The gray body model which we fit to the data, excluding the NIKA sources located near the SZ emission, allows us to better constrain the expected fluxes in the NIKA bands (see Adam et al. 2016, for more detail). And therefore, to produce a template to be removed from our data, as provided in figure 2 together with the radio contribution. Most of the model predictions are fully compatible with the NIKA observations. Only SMG11 at 150 GHz differ by more than $> 3\sigma$, and we note that we ~~except~~ indeed the NIKA measurement of SMG11 to be strongly contaminated by SZ emission because of its location. The SPIRE data are also well described by the model and we do not observe significant excess on the residual between the model and the data for any of the sources.

In addition to the radio source, F, the excess seen in the NIKA 260 GHz map coincide with SMG09 (northwest of sub-cluster D) and SMG05 (south of sub-cluster D). The corresponding SED peak at relatively low frequencies, indicating that these sources could be high redshift lensed galaxies. This is particularly true for SMG09, for which the SED peaks at about 600 GHz (500 μ m). Therefore, we search for counterparts to the NIKA detected sources in strong lensing HST data set (Hubble Space Telescope, Frontier Field campaign, see Diego et al. 2015). By requesting that the projected distance is less than 5 arcsec between our identified sources and that of HST, we find two possible candidates for SMG09 at $z = 4.5$ (R.A. +07:17:31.269, Dec. +37:44:41.10) at 2.0 arcsec from our coordinate, and $z = 3.0$ (R.A. +07:17:31.082, Dec. +37:44:42.36) at 2.5 arcsec from our coordinate (ID25.1 and ID62.1, respectively, Diego et al. 2015). The source SMG09 is, therefore, very likely to be a high redshift sub-millimeter galaxy lensed by MACS J0717.5+3745, or even the blending of two galaxies. In the case of SMG05, no counterpart is found even if we increase our threshold radius to 15 arcsec.

3.4. Diffuse sub-millimeter emission from the ICM

While galaxies are the major contributors to the sub-millimeter emission in galaxy clusters (Coppin et al. 2011), diffuse dust emission associated to the ICM could also lead to sub-millimeter emission (see, for example, Planck Collaboration et al. 2016, who study the overall contribution of dust in clusters). Such signal would likely be diffuse, at arcmin scales, and we expect it to be small compared to the galaxies, which give rise to emission on small scales. Using Herschel SPIRE maps toward MACS J0717.5+3745, we check that such signal is, at least, much lower than the one arising from point sources. Moreover, we do not observe any diffuse emission which would be correlated with the kSZ signal measured in section 5. Therefore, the dust contribution associated to the ICM is neglected in the NIKA bands in the following.

Table 4. Flux of the radio sources identified in the NIKA field, including the NIKA measurements. The model predictions at 150 and 260 GHz are also provided.

Frequency (GHz)	Source flux (mJy)						
	HT	B	F	C1	C2	C3	C4
0.235	573±7 ^(b)	100.93±0.80 ^(b)	63.17±3.00 ^(b)	—	1.95±0.50 ^(b)	—	29.64±0.70 ^(b)
0.610	109.8±3.2 ^(b)	44.79±2.60 ^(b)	30.29±0.50 ^(b)	—	0.98±0.05 ^(b)	—	0.15±0.05 ^(b)
1.365	22.2 ^(a)	19.9 ^(a)	—	—	—	—	—
1.435	22.4 ^(a)	18.8 ^(a)	6.46±0.15 ^(e)	1.37±0.15 ^(e)	—	2.03±0.15 ^(e)	—
1.485	20.0 ^(a)	18.3 ^(a)	—	—	—	—	—
1.665	18.1 ^(a)	18.3 ^(a)	—	—	—	—	—
4.535	4.7 ^(a)	7.0 ^(a)	—	—	—	—	—
4.885	3.9 ^(a)	6.4 ^(a)	—	—	—	—	—
8.460	0.7 ^(a)	1.9 ^(a)	—	—	—	—	—
28.5	—	2.28±0.25 ^(d)	3.29±0.19 ^(d)	—	—	—	—
30	—	1.60±0.17 ^(d)	2.70±0.17 ^(d)	—	—	—	—
90	—	—	2.8±0.2 ^(c)	—	—	—	—
150	N.A.	0.32±0.29 ^(f)	2.30±0.18 ^(f)	0.80±0.26 ^(f)	0.90±0.18 ^(f)	0.31±0.21 ^(f)	N.A.
260	N.A.	-0.24±1.15 ^(f)	1.82±0.72 ^(f)	0.81±1.04 ^(f)	0.44±0.73 ^(f)	0.39±0.86 ^(f)	N.A.
150 (model)	0.0050±0.0001	0.130±0.002	2.362±0.146	0.833±0.268	0.867±0.178	0.402±0.293	0.000±0.000
260 (model)	0.0021±0.0000	0.080±0.001	2.338±0.180	0.861±0.306	0.912±0.211	0.336±0.260	0.000±0.000

Notes. ^(a) VLA; [Bonafede et al. \(2009\)](#). ^(b) GMRT; [Pandey-Pommier et al. \(2013\)](#). ^(c) MUSTANG/GBT; [Mroczkowski et al. \(2012\)](#). ^(d) OVRO/BIMA; [LaRoque et al. \(2003\)](#); [Coble et al. \(2007\)](#). ^(e) FIRST; [Condon et al. \(1998\)](#). ^(f) NIKA; this work.

Table 5. Coordinates, measured fluxes and predicted fluxes in the NIKA bands for the eleven sub-millimeter sources identified in our field. The measured fluxes are from SPIRE ([Sayers et al. 2013](#)) and NIKA (this work).

Label	R.A. ^(a)	Dec. ^(a)	Measured fluxes (mJy)					NIKA prediction (mJy)	
			SPIRE (GHz) ^(a)			NIKA (GHz)		NIKA (GHz)	
			1200	857	600	260	150	260 (model)	150 (model)
SMG01	+07:17:32.11	+37:43:21.0	57.6±0.9	30.1±0.9	9.9±1.2	1.0±0.8	0.2±0.2	0.9±0.2	0.1±0.1
SMG02	+07:17:25.40	+37:47:05.7	25.2±0.9	14.7±0.9	1.3±1.4	0.7±1.3	-0.1±0.3	0.5±0.2	0.1±0.0
SMG03	+07:17:30.92	+37:46:50.6	15.2±0.9	13.9±0.9	6.2±1.2	0.1±0.9	0.6±0.2	0.8±0.2	0.1±0.1
SMG04	+07:17:34.91	+37:45:47.4	18.4±0.9	10.6±1.0	5.1±1.7	0.3±0.7	0.0±0.2	0.6±0.2	0.1±0.1
SMG05	+07:17:33.58	+37:44:01.9	14.3±0.8	16.8±0.9	13.3±1.2	1.3±0.7 ^(b)	0.2±0.2 ^(b)	1.8±0.3	0.4±0.1
SMG06	+07:17:25.06	+37:43:55.6	8.8±1.1	7.3±1.0	2.7±1.3	0.1±0.8	0.2±0.2	0.4±0.2	0.1±0.1
SMG07	+07:17:37.28	+37:45:34.1	12.1±0.9	12.7±1.0	14.1±1.2	0.1±0.7	0.4±0.2	1.6±0.3	0.3±0.1
SMG08	+07:17:30.87	+37:46:18.4	1.3±1.1	1.3±0.9	0.0±1.1	0.1±0.7	-0.1±0.2	0.0±0.0	0.0±0.0
SMG09 ^(c)	+07:17:31.24	+37:44:43.0	6.3±1.0	11.9±1.0	15.1±1.0	2.5±0.7 ^(b)	0.6±0.2 ^(b)	3.0±0.4	0.6±0.2
SMG10	+07:17:40.43	+37:45:26.7	4.2±0.9	5.3±0.8	3.1±1.2	-0.3±0.8	0.4±0.2	0.5±0.2	0.1±0.1
SMG11	+07:17:34.95	+37:44:33.1	4.7±1.1	4.8±0.8	4.9±1.4	0.0±0.7 ^(b)	-0.9±0.2 ^(b)	0.5±0.2	0.1±0.1

Notes. ^(a) From [Sayers et al. \(2013\)](#). ^(b) Likely to be contaminated by SZ. ^(c) High redshift lensed galaxy candidate with HST counterpart.

3.5. Construction of a mask for point sources

The spectral modeling of both radio and sub-millimeter point sources allows for a good first estimate of the contamination expected in our data. However, the model uncertainties are relatively large and once subtracted to the respective channels, we observe small residuals in the case of radio sources, that are visible in particular for sources that are outside the region dominated by SZ emission. This is likely due to our modeling being too simplistic since it does not account for the steepening of the radio spectrum, as discussed in section 3.2. Therefore, in addition to subtracting the point source model, we also construct a mask to avoid using pixels that we consider potentially biased when using the NIKA maps for photometry or for fitting purposes. This mask is constructed by applying a threshold on the best fit models at 150 and 260 GHz simultaneously. Such procedure is conservative and it is made possible taking advantage of the high angular resolution of the NIKA data. The mask we  is given on the right panel of figure 2.

4. X-ray data analysis

In the work presented in this paper, X-ray data are needed for two reasons. First, MACS J0717.5+3745 is known to be a very hot cluster ([Ma et al. 2009](#)) such that SZ relativistic corrections are expected to be fairly significant and have to be accounted for by using an extra estimate of the gas temperature, available from X-ray spectroscopy. Then, X-ray data are also needed in order to disentangle the gas line of sight velocity from the density and the temperature (see equation 5). Indeed, this cannot be done with the NIKA observations in two bands and an extra constraint is needed, which X-ray observations can provide.

4.1. Data preparation

MACS J0717.5+3745 was observed by the XMM-Newton telescope using the European Photon Imaging Camera (EPIC, [Turner et al. 2001](#) and [Strüder et al. 2001](#)) for 195 ks (obs-IDs 0672420101, 0672420201, and 0672420301) and by the *Chandra* Advanced CCD Imaging Spectrometer (ACIS,

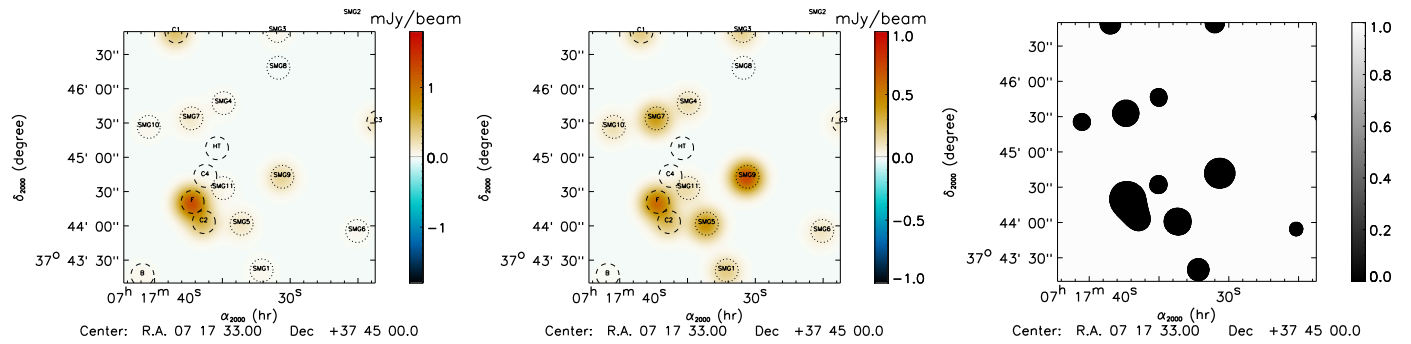


Figure 2. Point source model at 150 GHz (left) and 260 GHz (middle), and point source mask constructed from the 150 and 260 GHz point source models (right). The scale of the models is the same as in figure 1. We also provide the labels of each source, in dashed circles for radio sources and doted circles for sub-millimeter sources. The point sources subtracted maps can be seen in figure 7.

Garmire et al. 2003) for 250 ks in total (obs-IDs 800123, 800356, 801417, and 801432). We processed XMM-Newton datasets using the Science Analysis System (SAS) version 15.0.0 applying the latest version of calibration files available in March 2016. We processed Chandra datasets using the Chandra Interactive Analysis of Observation (CIAO) version 4.6.5 and calibration database version 4.7. Both datasets suffer from the contamination of high energy particle flux, namely the instrumental background. To reduce this component we removed from the XMM-Newton datasets all the events for which keyword PATTERN is > 4 and > 13 for MOS1,2 and PN cameras, respectively. We applied the Very Faint² (VF) mode filtering to obs-IDs 800356 and 801432. Since our background subtraction technique for Chandra can be applied only to observations taken using the VF mode, we removed obs-IDs 800123 and 801417 from our analysis, thus reducing the observation time available to 153 ks.

To remove observation intervals affected by flare episodes we followed the light-curve filtering procedures described in Pratt et al. (2007) and in the Chandra COOKBOOK³ for XMM-Newton and Chandra datasets, respectively. We removed from the analysis all the intervals where the count rate exceeded 3σ the mean value. We find no flare contamination in the Chandra dataset, so the full observation time of 153 ks was used. For the XMM-Newton dataset, the useful exposure times were 160 ks and 116 ks for MOS1,2 and PN cameras, respectively. We ran the wavdetect algorithm (Freeman et al. 2002) to identify point sources on exposure corrected images in the [0.3-2] keV and in the [0.5-2 ; 2-8 ; 0.5-8] keV bands for XMM-Newton and Chandra, respectively. Point source lists produced were inspected by eye, merged, and used as mask to remove point source contribution from the analysis. Point sources only detected by Chandra were masked from XMM-Newton dataset, using a circular region which radius was $15''$ within $3'$ from the aimpoint.

To perform spectral and imaging analysis using the same techniques we binned both datasets in sky coordinates and energy, creating an energy position photon cube following the technique described in Bourdin & Mazzotta (2008). To each event cube we assigned an effective area cube, which we use to correct for vignetting and exposure time, and the background noise cube. In the following, all the techniques described have been used for both Chandra and XMM-Newton datasets, unless stated otherwise.

We show in figure 3 the exposure vignetted corrected Chandra image in the [0.5-2.5] keV band and its wavelet denoised map in top left and right panel, respectively. As already found by several works (e.g. Zitrin et al. 2009, Ma et al. 2009, and Limousin et al. 2012), we can clearly see that this cluster exhibits a very complex dynamical activity with at least 4 sub-structures. Because of the ACIS higher resolution, we used Chandra datasets as baseline for imaging analysis purposes.

4.2. Background estimation

X-ray observation background can be divided in the sky and the instrumental component. For the latter we used the analytical models produced by Bourdin et al. (2013) and Bartalucci et al. (2014) for XMM-Newton and Chandra, respectively. We normalized both models selecting a region free from the cluster emission in the [10-12] keV and in the [9.5-10.6] keV band for XMM-Newton and Chandra, respectively. The sky component is due to a foreground Galactic component and a background extra-Galactic component. For the former we used two absorbed Astrophysical Plasma Emission Code (APEC, Smith et al. 2001) thermal models for which the temperatures are fixed to 0.248 keV and 0.099 keV (Kuntz & Snowden 2000). The extra-Galactic component was modelled using an absorbed power law with γ fixed to 1.42, as proposed by Lumb et al. (2002). We determined the normalization of all the components by performing a joint fit of the spectrum extracted from a region free of source emission. We noticed the presence of a small excess in the [0.3-1] keV band of XMM dataset, compatible with the solar wind charge exchange emission (Snowden et al. 2004). Even though the emission is due mainly to lines, we found that one absorbed APEC model at 0.86 keV is sufficient to reproduce the excess. We added this component in the joint fit. Once normalized, the background sky model is added to the instrumental one. Then, in all our spectral analysis procedures, we simply scale the resulting total background model by the ratio of the extraction areas.

4.3. Spectroscopy analysis

All X-ray spectral analysis are performed following the scheme described in Bourdin & Mazzotta (2008). For a given region of interest, we add to the background model a source emission model using an absorbed APEC, and fit it via χ^2 minimization to the spectrum, vignetted and exposure corrected, extracted from the photon cube. In all the X-ray fitting procedures described

² cxc.harvard.edu/cal/Acis/Cal_prods/vfbkgrnd

³ cxc.harvard.edu/contrib/maxim/acisbg/COOKBOOK

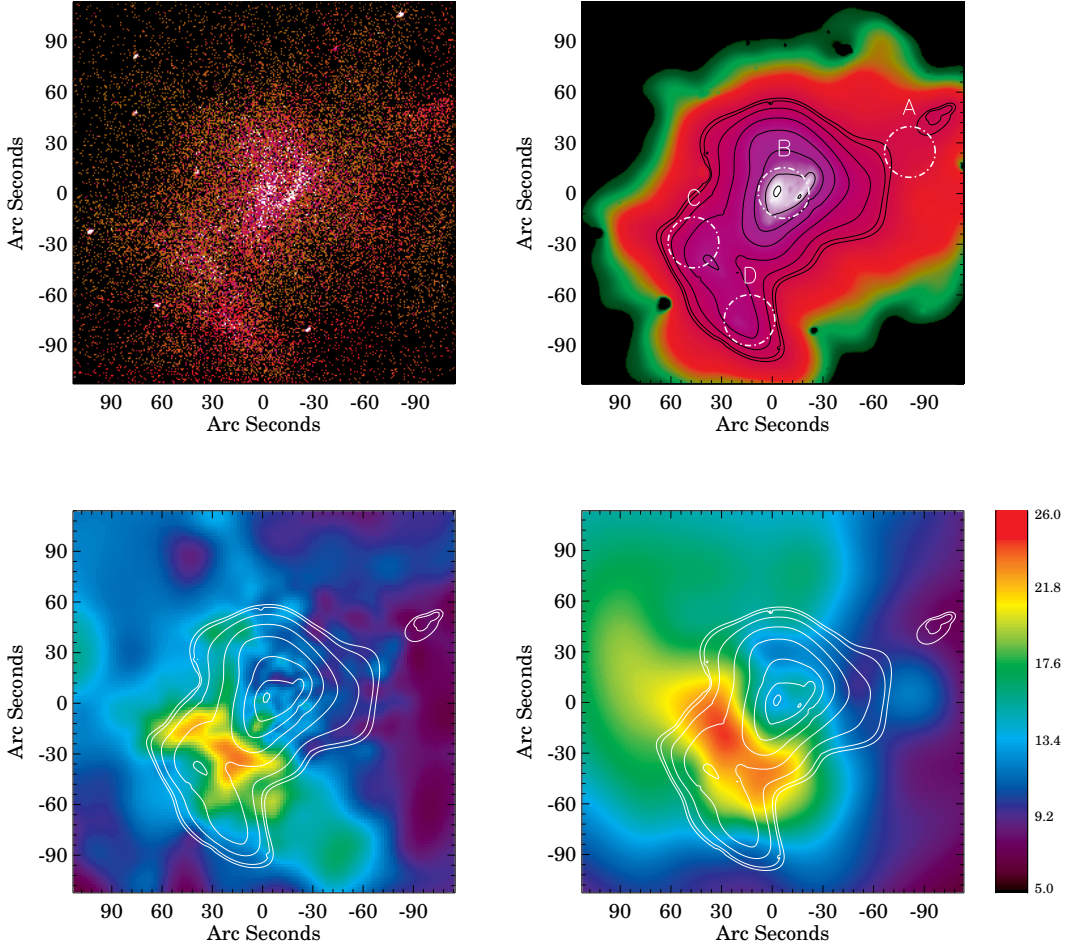


Figure 3. XMM-Newton and *Chandra* observations of MACS J0717.5+3745. **Top left panel:** *Chandra* exposure and vignetted corrected image in the [0.5-2.5] keV band. **Top right image:** wavelet de-noised map of the *Chandra* map shown in the top left panel. Iso contours are shown with black solid lines to enhance substructures. We report the four regions, highlighted with white circular regions, from table 2. **Bottom left image:** XMM-Newton temperature wavelet de-noised map using a threshold cut of 1σ . Contours from the wavelet map are overlaid using white contours. **Bottom right image:** same as bottom left panel except that we show the temperature map computed using the *Chandra* dataset. All the maps shown are centered on the X-ray peak. The color scale indicates the temperature in keV.

in this work, the absorption is fixed to the Galactic value along the line of sight $n_H = 6.63 \times 10^{-20} \text{ cm}^{-2}$, as determined from the LAB survey (Kalberla et al. 2005). All the models are convolved by the appropriate response matrix files, accounting for energy resolution loss due to instrumental effects. The source emission model and the sky background models are multiplied by the appropriate ancillary response file. From the fitting procedures performed in the [0.3-10] keV and [0.7-10] keV band for XMM-Newton and *Chandra*, respectively, we determined the APEC model temperature, abundance and normalization.

We produce temperature maps applying the wavelet filtering algorithm described in Bourdin et al. (2004) and in Bourdin & Mazzotta (2008). Briefly, we sample the field of view in square grids where each unitary element increases by powers of 2. The minimum size of the meta-pixel being defined so that it contains at least 200 photons. In each meta-pixel we extract the spectrum and measure the temperature, fixing the abundance to 0.3 solar value, obtaining a first set of temperature and associated fluctuation maps. We then convolved these maps with a B2-spline function evaluated at different scales to obtain the corresponding wavelet coefficients. To construct a de-noised temperature map

we applied a threshold of 1σ to each wavelet coefficient map. We show in figure 3 the temperature maps that we obtained from XMM-Newton and *Chandra* datasets, in the left and right bottom panel, respectively. We can see that both temperature maps identify the same hot structure with temperatures of the order of ~ 24 keV. Furthermore, we can see that there is a cold region in the North-West sector associated with the most prominent structures.

As an additional test to check the validity of the values of the temperatures maps, following Wang et al. (2016), we extracted the spectra from the four circular regions shown in the top right image of figure 3, using a circular radius of $15''$ and $30''$. We then measured the temperatures via our fitting procedure. We report in table 6 the measured temperature and the associated errors at 1σ . Because of *Chandra* lower exposure time and sensitivity, we measure the temperature only in the $30''$ circular bin aperture. The values reported for the two instruments are consistent with the values found in the respective temperature maps. As expected, *Chandra* measures higher temperatures with respect to XMM-Newton (see, e.g., Martino et al. 2014; Schellenberger et al. 2015), but consistent within the errors. From now, because

Table 6. X-ray spectroscopic temperature of the four sub-clusters in MACS J0717.5+3745, centered on the regions defined in table 2.. The temperature are provided for both XMM-Newton and Chandra data for 30" apertures radius and we also provide the values for 15" radius in the case of XMM-Newton.

Sub-cluster	XMM-Newton (15")	XMM-Newton (30")	Chandra (30")
A	$7.57^{+1.62}_{-1.23}$ keV	$7.71^{+0.78}_{-0.68}$ keV	$9.29^{+2.20}_{-1.48}$ keV
B	$10.70^{+1.12}_{-0.88}$ keV	$11.22^{+0.68}_{-0.61}$ keV	$13.33^{+1.59}_{-1.28}$ keV
C	$16.39^{+3.48}_{-2.60}$ keV	$18.09^{+2.01}_{-1.78}$ keV	$17.82^{+3.62}_{-2.73}$ keV
D	$12.55^{+2.75}_{-1.92}$ keV	$13.56^{+1.82}_{-1.38}$ keV	$16.31^{+4.73}_{-2.78}$ keV

of the better resolution and significance, we use XMM-Newton spectroscopic results as our baseline.

5. A map of the kinetic Sunyaev-Zel'dovich signal

In the case of pure tSZ signal with small relativistic corrections, we expect the signal to be proportional at any frequency. However, this is clearly not the case for the NIKA data such that another contribution is necessary to explain our observations. Motivated by the results of Ma et al. (2009), Mroczkowski et al. (2012) and Sayers et al. (2013), we assume that the observed signal is due to the tSZ and the kSZ effects, and we use the NIKA data to disentangle the two. The main goal of this section is, therefore, to produce, for the first time, a map of the kSZ effect. This constitutes the main result of this paper.

5.1. Reconstruction of the kinetic Sunyaev-Zel'dovich signal

The two NIKA maps, cleaned from astrophysical contaminant, provide a measurement of the surface brightness, ΔI_ν , in the different regions of the cluster. The sensitivity to the tSZ and the kSZ contributions are known from the coefficients given in table 1, and are corrected for each pixel of the sky from relativistic effects using the XMM-Newton X-ray spectroscopic temperature map of figure 3, under the assumption that the temperature is constant along the line of sight (see section 4). We can therefore invert equation 3 in order to separate the contribution of the tSZ signal, given by

$$y_{\text{tSZ}} = \frac{g(\nu_1, T_e) \Delta I_{\nu_2} - g(\nu_2, T_e) \Delta I_{\nu_1}}{I_0 g(\nu_1, T_e) f(\nu_2, T_e) - I_0 g(\nu_2, T_e) f(\nu_1, T_e)}, \quad (6)$$

and that of the kSZ signal,

$$y_{\text{kSZ}} = \frac{f(\nu_1, T_e) \Delta I_{\nu_2} - f(\nu_2, T_e) \Delta I_{\nu_1}}{I_0 f(\nu_1, T_e) g(\nu_2, T_e) - I_0 f(\nu_2, T_e) g(\nu_1, T_e)}. \quad (7)$$

We propagate the noise through Monte Carlo realizations as discussed in section 2.2, including the CIB contribution and its induced correlation between the two NIKA frequencies. The statistical errors on both tSZ and kSZ are largely dominated by the noise at 260 GHz due to the intrinsic sensitivity of this band and its spectral location.

5.2. Reconstruction of the kinetic signal toward sub-clusters

We first consider the mean surface brightness measured in the individual regions provided in table 2, i.e., within 22 arcsec radius disks. The point source mask was applied before computing the brightness. The results are presented in figure 1 for the four sub-clusters. Following section 5.1, we use these measurements to constrain the amplitude of both the tSZ and kSZ spectra, as shown in figure 4. From equations 3 and 5, we can see that a

positive kSZ amplitude corresponds to a negative line of sight velocity, which means that the cluster is moving toward the observer, with respect to the CMB reference frame. The signal to noise is too low in region A and both tSZ and kSZ amplitudes are compatible with zero. As the two are degenerated, however, the 150 GHz band is nonetheless not compatible with zero and therefore, we detect tSZ emission in region A if we assume that the kSZ signal is negligible. In region B, we detect tSZ and kSZ emission at 2.6σ and -4.6σ , respectively. Moreover, we find that the kSZ induced brightness is slightly larger than that of the tSZ, at the scales probed by NIKA. The kSZ signal is negative, which explains the decrement observed in this region at 260 GHz with respect to the 150 GHz expectation. In region C, we significantly detect tSZ signal and find indication for kSZ signal at 7.8σ and 2.1σ , respectively, but the situation is reversed with respect to region B and the kSZ emission is positive. The tSZ signal strength is very high, in agreement with the expectation from the merger scenario, responsible for gas heating in this region. This is also in agreement with our X-ray derived temperature map. Finally, tSZ emission is detected in region D at 4.3σ and the kSZ significance is 0.6σ .

5.3. Mapping of the kSZ and tSZ signal

The results of section 5.2 provide quantitative illustration of our constraints, but they directly depend on the choice of the region coordinates and their aperture size. Therefore, we now consider the full surface brightness NIKA data (in addition to the XMM-Newton temperature map for relativistic corrections) and we use them to compute maps of the tSZ and kSZ amplitude, i.e., maps of y_{tSZ} and y_{kSZ} , that are independent of our basic regions. The residuals of point sources are not considered here, but the obtained maps are compared to the mask to check that the kSZ signal we detect is not affected by point sources. Before combining the two data sets, we convolve the NIKA maps to the same angular resolution, i.e., 22 arcsec. The resulting maps are provided in figure 5. We observe a tSZ peak coincident with the region of sub-cluster C, as expected and already discussed. The peak signal to noise is reaching 7.3σ , which is more than twice smaller than on the 150 GHz map due to the noise introduced by the 260 GHz data. The signal is more diffuse in the other regions but it covers all the cluster extension. The kSZ map shows two distinct peaks of opposite sign and of similar amplitudes, reaching -4.9 and $+3.4\sigma$, respectively. The negative peak is almost coincident with region B and the positive one is located at the northeast edge of region C. No kSZ signal is significantly detected near sub-clusters A or D. Similarly, we do not observe diffuse large scale kSZ signal that would results from the motion of the overall cluster and sub-clusters.

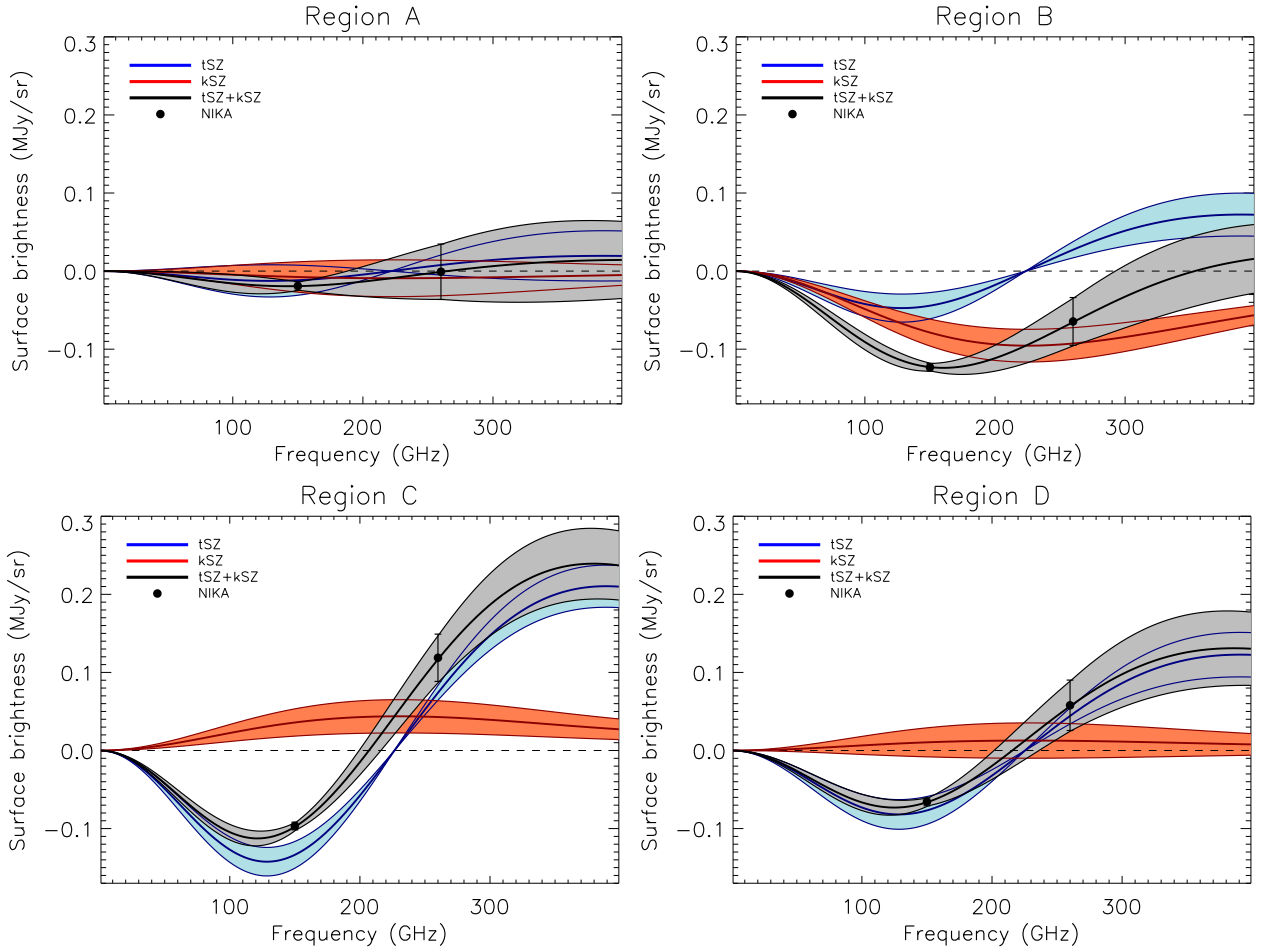


Figure 4. Constraints on the kSZ and the tSZ amplitudes toward the four sub-clusters (from A to D). The black data points provide the average brightness measured by NIKA in the 22 arcsec radius regions with center coordinates given in table 2 and shown on figure 1. The shaded areas give the 68% confidence level constraints on the kSZ (red), the tSZ (blue) and the sum of the two (gray). Possible point source residuals were masked when computing the average surface brightness.

5.4. Systematic effects

In addition to the noise and to the astrophysical contaminants, which we account for as discussed in section 3, our measurement is affected by three main systematic effects which we discuss here.

The first one is due to the absolute calibration uncertainties of the NIKA data. A change in the absolute calibration directly impact the kSZ measurement since it changes the relative weights of the two NIKA bands. Assuming a typical gas temperature of 10 keV, equations 6 and 7 can be expressed as $y_{\text{tSZ}} \propto -0.38 \times \Delta I_{\nu_2} + 0.62 \times \Delta I_{\nu_1}$ and $y_{\text{kSZ}} \propto 0.20 \times \Delta I_{\nu_2} + 0.80 \times \Delta I_{\nu_1}$, where the numerical coefficients indicates the fraction of the maps at 260 GHz and 150 GHz that contribute to the tSZ and kSZ maps. We can see that changing our 150 GHz calibration by 7% (the calibration uncertainty), leads to a change of 2.7% for the tSZ map, and 1.4% for the kSZ map. Similarly, changing our 260 GHz calibration by 12% leads to a change of 7.4% for the tSZ and 9.6% for the kSZ map. While the absolute calibration uncertainty does not significantly affect the level of detection, it can slightly change the relative strength of the signal in the different regions. If we focus on the kSZ map in region B and C, we can notice that the 150 GHz surface brightness is negative in both regions, while it changes sign at 260 GHz, being negative in region B. On the other hand, the two linear coefficients that

are used to compute the kSZ map from the primary NIKA maps (0.20 and 0.80 as written above) are both positive. Therefore, if the calibration changes in the same direction at both frequencies, the changes will add up in region B, and they will cancel each other in region C. Similarly, if the calibration changes are opposite in sign, they will cancel each other in region B, and they will add up in region C. Therefore, summing the calibration uncertainties, the kSZ signal in region B can increase (or decrease) by 11.0% while it increases (decrease) only by 8.2% in region C. Symmetrically, the same is true when inverting B and C. Note that we apply a simple sum of the calibration errors instead of a quadratic sum because they are likely to be strongly correlated. This effect will propagate linearly to the constraint on the line of sight velocity in section 6, but it is small compared to the statistical uncertainties. A similar reasoning can also be done for the tSZ map.

The second systematic effect is due to the uncertainty in the derived X-ray temperature and the assumption that the temperature is constant along the line of sight. In order to estimate how changes in the temperature affect our results, we reproduce the kSZ map applying a 2% change in the normalization factor of the temperature map. We also add gaussian noise of amplitude 3 keV at a resolution of 2 arcsec. Due to the fact that the relativistic corrections are close to be proportional in the two NIKA bands, the changes in the temperature map lead to only small

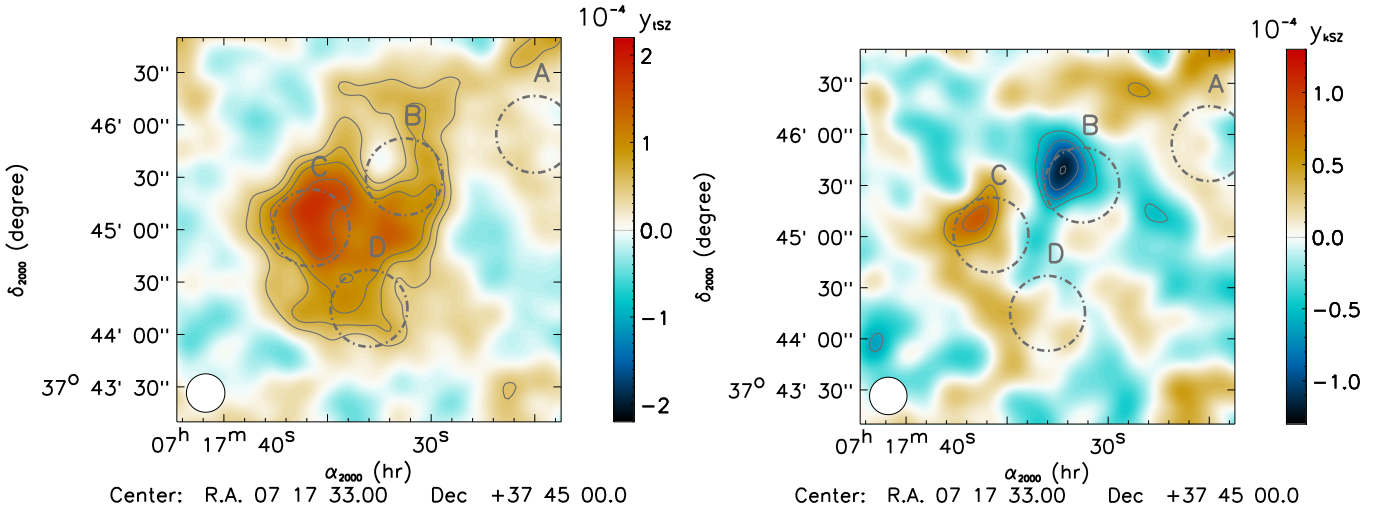


Figure 5. Map of the thermal SZ effect, y_{tSZ} (left), and the kinetic SZ effect, y_{kSZ} (right). Gray contours are multiples of 1σ , starting at $\pm 2\sigma$. The map effective resolution, 22 arcsec, is shown as a white circle on the bottom left corner. Sub-cluster regions are also represented in white.

changes in the kSZ detection level, i.e., less than 0.15σ . The absolute amplitude of the signal, however, is affected by up to 0.4σ changes at the positive peak, which correspond to a hot gas in region C, where relativistic effects are important.

The third systematic effect is due to the large angular scale filtering that affect the NIKA data. The filtering is the same in the two bands, and as the quantities y_{tSZ} and y_{kSZ} are a linear combination of the two NIKA maps, they are affected by the same filtering. Therefore, the tSZ and kSZ reconstructed signal are smoothly dimmed at scales larger than ~ 2 arcmin. However, the kSZ signal we observe is much more compact than the one induced by the tSZ effect, such that we expect this effect to be less important here than for tSZ observations. The

5.5. Comparison to other wavelengths

In figure 6, we compare the kSZ mapping obtained with NIKA to other wavelengths, the as tracers of the different cluster components. We use Chandra X-ray photon count (obs-ID 4200) as a proxy for the gas distribution ($\propto n_e^2$), HST optical imaging (CLASH data, Postman et al. 2012) to identify the galaxy spatial distribution, and strong lensing mass reconstruction to probe the dark matter (Zitrin et al. 2011).

The ray image presents two main peaks in region B. The most significant one is located on the east side of the region (hereafter B1) and the second one on the west side (hereafter B2), the two being separated by about 20 arcsec. The group of galaxies associated to sub-cluster B is on overall more coincident with B2, even if galaxies are also observed around B1. The dark matter follows well the main galaxies, and is therefore better aligned with B2. The negative kSZ signal coincides well with the main X-ray clump, but is significantly offset with respect to the secondary peak. The morphology of clump B2 is that of an arc (or a tail) around the dense core, similar to what can be observed in mergers on the plan of the sky (e.g., Clowe et al. 2006, for the bullet cluster), which would suggest, if this is the case, that B2 is moving perpendicular to the line of sight and is not responsible for kSZ emission. Our kSZ data together with X-ray imaging therefore suggest that sub-cluster B could itself be made of two relatively independent sub-clusters. The main one, B1, is rapidly moving along the line of sight, while the second

one, B2, could be the moving mostly perpendicular to the line of sight, after having interacted with the main cluster.

The positive kSZ signal coincides well with the northern half of the galaxies associated with sub-cluster C, while the other half of the galaxies are coincident with no kSZ detection. The X-ray peak is centered on the southern part of the galaxy group and the shift between the kSZ peak and the X-ray peak is about 20 arcsec. As this sub-cluster is highly disturbed, we can expect strong inhomogeneities in the gas velocity distribution, as suggested by our data, but any further interpretation would require higher signal to noise kSZ imaging. Nonetheless, it is worth noting that the velocity dispersion within this sub-cluster is very high (1761^{+234}_{-607} km/s for 10 redshifts, see Ma et al. 2009), which could also suggest that the underlying distribution is multimodal.

No kSZ signal is detected around sub-cluster D but we notice a shift between the gas and the brightest galaxies and dark matter, the gas density peak being about 25 arcsec shifted to the south with respect to the other component.

Sub-cluster A is not well identified in X-ray, but the galaxy and dark matter location are consistent.

Finally, the foreground radio galaxy is visible in X-ray, but also in optical, as the bright source SE with respect to region C.

6. Constraints on the gas line of sight velocity distribution of MACS J0717.5+3745

The detection of the kSZ effect implies the detection of gas motion, and opens the possibility to study the velocity distribution of the gas contained within the cluster. We detect positive line of sight gas velocity in the direction of sub-cluster B, i.e., the gas is moving away from us in the CMB reference frame, and negative gas line of sight velocity toward sub-cluster C, i.e. the gas is moving toward us. However, measuring the absolute line of sight velocity from our kSZ map requires to disentangle from the integrated line of sight density, accounting for projection effects, and this cannot be done from our SZ observations alone. Therefore, in this section, we model the cluster gas distribution in terms of electronic density and gas line of sight velocity, and we fit our data using extra information from X-ray spectroscopic temperature. Unlike results presented in section 5, the results we present in this section are therefore dependent of the model we use to describe the cluster. In particular, we stress

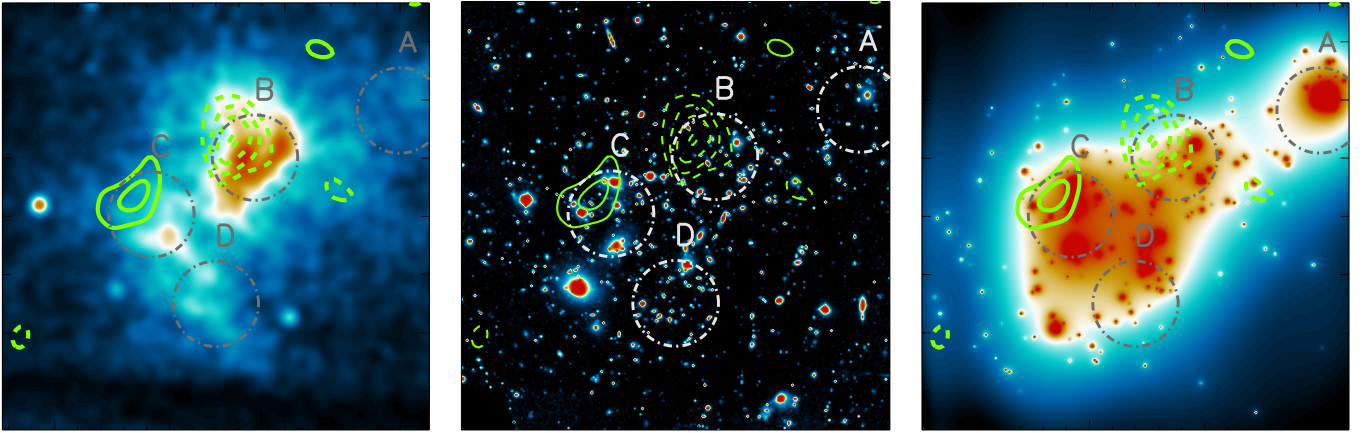


Figure 6. Comparison between the kSZ signal and other probes of the cluster components, shown on saturated linear scales. The frames are the same as the ones of figure 5, and the Chartreuse contours reproduce the kSZ signal to noise, given as a solid line if positive ($+2\sigma$ and $+3\sigma$) and dashed line if negative (-2σ , -3σ and -4σ). Our reference regions are provided as grey circles. **Left:** Chandra X-ray photon count image, smoothed to 7 arcsec FWHM. **Middle:** HST optical combined image from the CLASH data (Postman et al. 2012). **Right:** Lensing mass (κ) from Zitrin et al. (2011).

that any mis-modeling of the gas density, which is intrinsically subject to strong assumptions for such a complex object, will reflect in the optical depth that is itself degenerated with the gas line of sight velocity.

6.1. Physical modeling of the gas distribution of MACS J0717.5+3745

As discussed in section 1, MACS J0717.5+3745 is known to be multimodal with four main sub-clusters. Therefore, we model the cluster by a set of four spherically symmetric clumps describing the gas distribution associated to each sub-cluster. We model each density profile by a β -model (Cavaliere & Fusco Femiano 1978),

$$n_e^{(i)}(r) = n_{e0}^{(i)} \left[1 + \left(\frac{r}{r_c^{(i)}} \right)^2 \right]^{-3\beta^{(i)/2}}, \quad (8)$$

where i labels each sub-cluster. We also assume that the sub-clusters are all isothermal, with a gas temperature $T_x^{(i)}$ estimated from X-ray spectroscopy, as reported in table 6. As our baseline, we use the XMM-Newton values obtained within 30 arcsec radius apertures. The line of sight gas velocity of each sub-cluster is also assumed to be a constant, i.e. each clump has its own bulk velocity.

The NIKA surface brightness maps are the primary observables to which we compare our model, and they are modeled as

$$\begin{aligned} \frac{\Delta I_\nu^{\text{model}}}{I_0} \Big|_{mn} &= \sigma_T \sum_i f_\nu(T_x^{(i)}) \frac{k_B T_x^{(i)}}{m_e c^2} \int n_e^{(i)} dl \Big|_{mn} \\ &+ \sigma_T \sum_i g_\nu(T_x^{(i)}) \frac{-v_z^{(i)}}{c} \int n_e^{(i)} dl \Big|_{mn}, \end{aligned} \quad (9)$$

where $T_x^{(i)}$ and $v_z^{(i)}$ are scalar quantities. The line of sight integrations are computed analytically for each sky pixel (m, n) , as

$$\int_{-\infty}^{+\infty} n_e^{(i)} dl = \sqrt{\pi} n_{e0}^{(i)} r_c^{(i)} \frac{\Gamma(\frac{3}{2}\beta^{(i)} - \frac{1}{2})}{\Gamma(\frac{3}{2}\beta^{(i)})} \left[1 + \left(\frac{R_{mn}^{(i)}}{r_c^{(i)}} \right)^2 \right]^{\frac{1}{2} - \frac{3\beta^{(i)}}{2}}, \quad (10)$$

where R is the projected radius from each sub-cluster centers and the quantity $\Gamma(t)$ represents the Gamma function. Since the SZ surface brightness depends linearly on the electronic density, the contribution of each sub-cluster is summed regardless of cross terms that would appear otherwise (e.g., for the X-ray surface brightness, which depends on n_e^2). This allows us to ignore the exact coordinate of each sub-cluster along the line of sight. The projected location of the sub-clusters centers, however, are parameters of our model.

6.2. Fitting algorithm

In order to fit parameters of our model, we need to compare our data to the expected simulated signal according to the values of the parameters and to the description of the gas discussed in section 6.1. The fitting approach we use consists in processing the test simulations through the same observational effects that affect our data, in order to predict the observable signal that we can directly compare to the SZ surface brightness maps. The SZ simulated maps are convolved to the beam and the transfer function of the NIKA processing. We also account for the zero level of the maps individually using two nuisance parameters, because they are not constrained by the NIKA observations. The parameter space is sampled using Monte Carlo Markov Chains (MCMC). The Metropolis-Hastings algorithm (see, e.g., Chib & Greenberg 1995) is used to define the evolution of the chains, by using the gaussian log likelihood computed as

$$\mathcal{L} \propto \sum_{m,n} (\Delta I_{\text{NIKA}}^{\text{data}} - \Delta I_{\text{NIKA}}^{\text{model}})_m (C_{\text{NIKA}}^{-1})_{m,n} (\Delta I_{\text{NIKA}}^{\text{data}} - \Delta I_{\text{NIKA}}^{\text{model}})_n, \quad (11)$$

where subscript NIKA stand for the joint 150 GHz and the 260 GHz data. The quantity C_{NIKA} is the full noise covariance matrix of the NIKA surface brightness maps, including the noise correlation between the two bands. Pixels that are potentially contaminated by point source residuals are masked so that they do not contribute to the likelihood.

Our model includes a total of 26 parameters (4×3 for the density, 4 for the line of sight velocity, 2×4 for the coordinates, and 2 for the zero level of the maps). Even if the model describing each sub-cluster is relatively simple, the overall complexity of the cluster, and in particular the degeneracy between the char-

acteristic radius, the slope parameters, and the exact sub-cluster centers that are not well determined, does not allow us to let all parameters free. In particular, the slopes of the density profile are not well constrained by our data. Therefore they are varied but limited to the range [1/3, 3]⁴, in order to marginalize on their uncertainties and avoid diverging chains in the MCMC. We also apply a 10 arcsec standard deviation gaussian prior on the coordinates of the sub-clusters, centered on the coordinates given in table 2. The model being symmetric under the permutation of sub-clusters, this measure to avoid mixing between the different clumps, but we check a posteriori that the best-fit coordinates are consistent with our prior values.

In the case of sub-cluster A, the signal observed is almost consistent with noise at the 3σ level at 150 GHz and is not detected at 260 GHz. The velocity, which is fully degenerated with the gas density, can therefore be constrained in principle, but it is allowed to explore the range $[-\infty, +\infty]$ at the 3σ level. This prevents the MCMC sampling of the posterior likelihood to converge. Therefore, we do not fit for the velocity of sub-cluster A and set $v_z^{(A)} = 0$.

The convergence of the chains are verified using the Gelman–Rubin convergence criteria (Gelman & Rubin 1992). After convergence, we remove a burn-in phase and we account for the correlation length of the chains. Finally, the chains histograms provide the probability density function in the parameter space.

6.3. X-ray prior on the gas density

The fitting algorithm of section 6.2 does not use X-ray imaging information because the latter suffers from projection effects that are not accounted for in our model. Indeed, our model would require additional parameters to predict the expected X-ray surface brightness because, unlike SZ images, X-ray requires the knowledge of the relative coordinate of the sub-clusters along the line of sight. This is due to cross terms between sub-clusters, which appear when squaring the density, and would be responsible for additional emission on large scales. However, NIKA SZ data alone are subject to strong degeneracies between the line of sight velocity and the optical depth, which can be broken with additional information from X-ray. This can improve significantly the constraint on the gas velocity, but at the cost of extra assumption on the line of sight geometry of the cluster.

In the following, we therefore consider two cases when fitting the model of section 6.1 to our data.

- As our baseline, hereafter F1, we do not consider X-ray imaging. The fit relies only on SZ imaging and X-ray estimates of the gas temperature. In this case, we do not use all the available information to constrain the velocity, but we are not significantly affected by assumptions concerning the line of sight distribution of the gas.
- The second fit, hereafter F2, makes use of extra information from X-ray imaging. In this case, we consider the deprojected XMM-Newton density profile centered on the X-ray peak (extracted as in Adam et al. 2016), i.e. within a few arcsec of region B. We fit the profile with a β -model and use the constraint obtained on n_{e0} (the parameter that is the most degenerated with v_z) as a prior in the fit described in section 6.2. Such approach is only possible toward sub-cluster B because any density profile extraction in the other regions,

⁴ The lower limit is required from equation 10, since the argument of the Gamma function, $\frac{3}{2}\beta^{(i)} - \frac{1}{2}$, must be larger than zero.

i.e. away from the X-ray peak, would strongly affected by deviation from spherical symmetry.

While fit F1 is conservative, fit F2 allows us to break the $v_z - \tau$ degeneracies, and check the consistency between our SZ based constraint and X-ray data.

6.4. Constraints on the velocity

The results of the MCMC fit F1, i.e. without the X-ray prior, is provided in figure 7, showing the input data, the maximum likelihood model, and the residual between the two. Despite the complexity of the cluster, a simple multi-component β -model is able to reproduce the SZ surface brightness data very well.

The 150 GHz residual map is mostly consistent with noise and we observe only little features exceeding 2σ . Nevertheless, we see a -3σ negative excess in the direction of the foreground galaxy F, indicating that our radio model predicts a flux higher than expected. This is in agreement with the fact that we have neglected the possible steepening of its spectrum at high frequencies. The corresponding pixels where make in the fit.

The 260 GHz map is also mostly consistent with noise, but again, we observe a negative residual on the west of region C, while the east residual of region C is positive. It might indicate that the velocity distribution in region C is not constant, as hinted already by the comparison between the kSZ map itself and data at other wavelengths. We also notice that the shape of our model for sub-cluster B is too extended compared to the 260 GHz data. It results in positive residual around the kSZ peak, and negative residual at the peak location. This could be due to the fact that sub-cluster B itself is made of two sub structures, as discussed previously. Both B1 and B2 give rise to tSZ emission so that the signal at 150 GHz is relatively extended, while the kSZ, dominant at 260 GHz, is only seen toward B2, which would lead to a more compact signal than the one at 150 GHz. Another alternative explanation could be that the constant temperature assumption is not valid. The latter implies that the pressure (related to the tSZ) and the density (related to the kSZ) have the same radial dependence, from the ideal gas law. Since the extension of the model is widely driven by the 150 GHz map, itself strongly affected by tSZ emission, our constant temperature assumption will result in a density profile less compact than the true one, if sub-cluster B is a cool-core system, as expected from Ma et al. (2009). At 260 GHz, channel which is largely dominated by kSZ emission, the model will therefore be more extended than expected. This is what we observe, and it is certainly one of the limitation of our model.

The MCMC chains are used to compute the optical depth at the center of each sub-clusters, expressed as

$$\tau_0^{(i)} = \sqrt{\pi} \sigma_T n_{e0}^{(i)} r_c^{(i)} \frac{\Gamma\left(\frac{3}{2}\beta^{(i)} - \frac{1}{2}\right)}{\Gamma\left(\frac{3}{2}\beta^{(i)}\right)}. \quad (12)$$

This is the quantity that reflects the most the degeneracy between the ICM density distribution and the line of sight velocity (see equation 5). Figure 8 provides the posterior probability density function in the line of sight velocity versus central optical depth plane for each sub-cluster B, C and D. The one dimensional marginalized distribution are also provided as histograms.

As expected, we observe a strong degeneracy between $\tau_0^{(i)}$ and $v_z^{(i)}$ for all the sub-clusters in our baseline fit F1 (in blue). This degeneracy is broken in the case of F2, when using priors (sub-cluster B only) on the X-ray density, and the constraint are

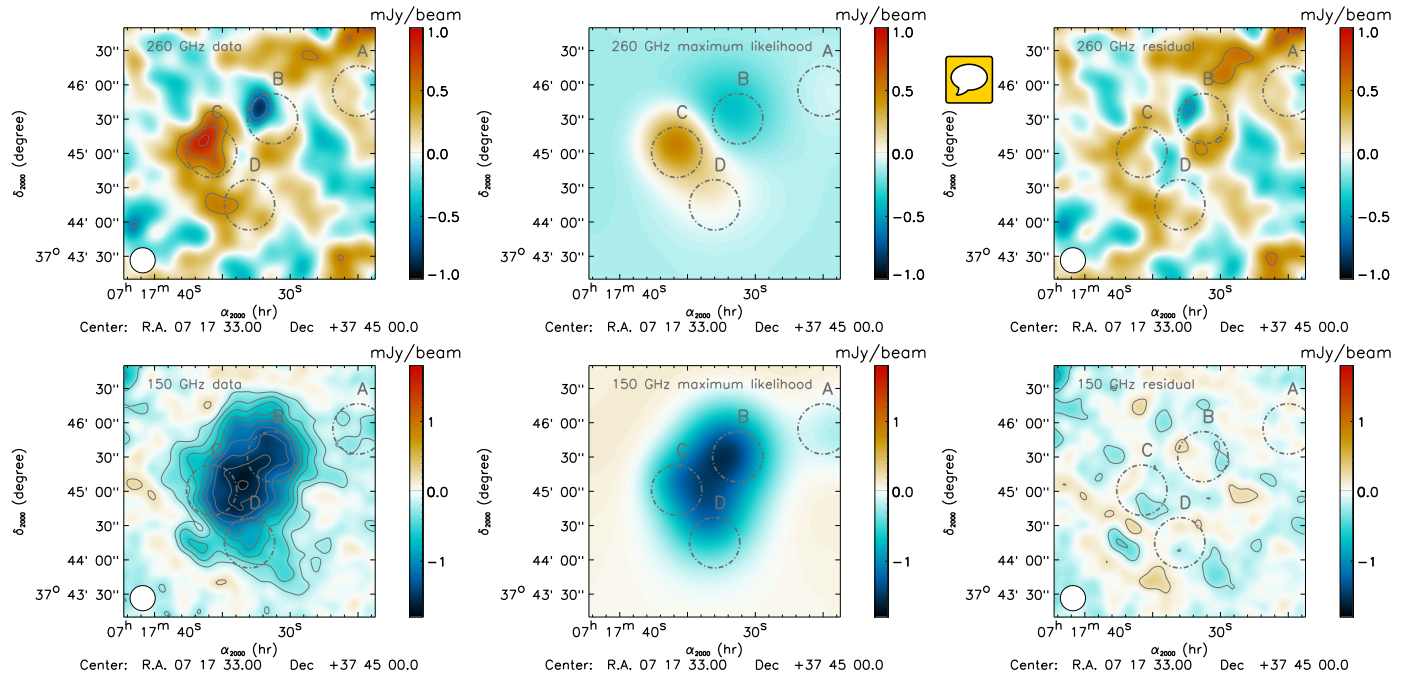


Figure 7. Comparison between the data and the best fit model (F1). From left to right, the figure shows the input data, the best fit model, and the residual. The top row provides the 260 GHz data and the bottom row the 150 GHz data. Contours are the same as figure 1.

significantly improved (in red). While the line of sight velocity is fully compatible with zero for sub-cluster D, sub-cluster B and C present distributions that are significantly different from zero, therefore excluding null velocity as expected from our kSZ map.

The constraint from F1 and F2 are consistent, as reported in figure 8 (sub-cluster B), and the residual with respect to the best fit is not significantly degenerated. This indicates that the SZ data as described by our model are not in contradiction with respect to X-ray imaging. Nevertheless, we observe a small tension (less than 2σ) in the case of sub-cluster B between the fits F1 and F2. As discussed several times, this could be due to sub-cluster B being made of two sub-components, with only one of them having a strong line of sight velocity. The X-ray prior forces the model to account for the density of both sub-components leading to a smaller line of sight velocity. In the case of F1, i.e. without X-ray prior, this effect is absorbed in the degeneracy.

The best fit line of sight velocity and their errors are reported in table 7.

In addition to the central optical depths, our model allows us to compute the overall optical depth map of the cluster for each sky pixel. This map is not independent of the best fit velocity because of the $\tau_0^{(i)} - v_z^{(i)}$ degeneracies, but it does not depend significantly on the velocity modeling because the data are dominated by tSZ signal (i.e., density and temperature), and the velocity accounts only for a relatively small correction to our model. Therefore, we can use it together with our kSZ map to break the degeneracy of equation 5 and obtain a map of the gas line of sight velocity in MACS J0717.5+3745. Such a map can be used to identify structure in the velocity and assess the validity of our assumption about the velocity being constant in each region. The optical depth map and the line of sight velocity maps are shown in figure 9 for both fit F1 and F2. The kSZ map is associated to statistical uncertainties, while the optical depth model gives rise to a systematic effect which is not accounted for in the velocity map. Therefore, the error contours provide the signal to noise but they do not reflect the true uncertainty of the map be-

cause it depends on the model we use. In particular, the constant temperature assumption can affect the extension and amplitude of the clumps in the optical depth map. As the noise of the velocity map increases with decreasing optical depth, we mask pixels for which the noise is boosted by a factor larger than three, with respect to the minimum noise of the map. We therefore focus on the cluster brightest regions.

In the case of our baseline fit, F1 (left panels), the optical depth presents a smooth structure which is maximum in region C, reaching about 1.5×10^{-2} . This is counter intuitive with respect to the X-ray imaging where the peak is clearly located toward sub-cluster B. The X-ray imaging being sensitive to n_e^2 , this could indicate that sub-cluster B is highly peaked while sub-cluster C is more diffuse and extends further in space. Our best fit model F1 being limited by degeneracies, we check this result by computing the best fit model F2 (right panels), i.e. when using the X-ray density prior. In this case, the optical depth map increases toward sub-cluster B by about 40%, and its value between sub-cluster B, C and D becomes almost constant. Nonetheless, we do not observe a peak toward sub-cluster B and our model suggests that it is much more compact than sub-clusters C and D. On the velocity map, we observe a dipolar distribution associated to sub-clusters B and C. Its significance is the same as the one observed on the kSZ map. The map is mostly negative between regions B and D but it is not significant. We observe a strong gradient between the north east and the south east of region C. This is consistent with group C having a complex velocity structure. We note that in the case of the fit F2, the velocity toward sub-cluster B reduces by about 40%. The dipolar structure becomes therefore more symmetrical in terms of amplitude, but the structure remains very similar. We also note that unlike the optical depth model, the velocity map is convolved to the NIKA transfer function similarly to the kSZ map.

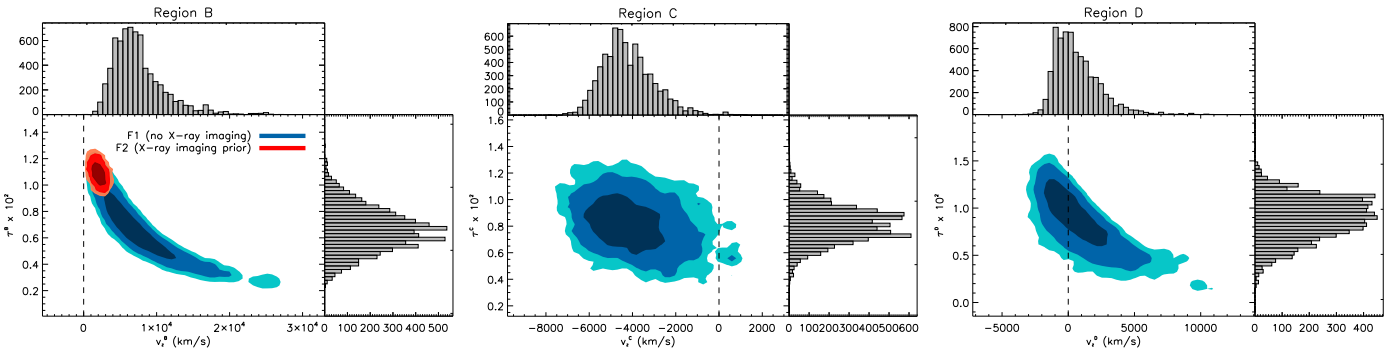


Figure 8. Constraints of the model on the ICM distribution in the plane line of sight velocity – central optical depth, $v_z^{(i)} - \tau_0^{(i)}$, for sub-clusters B, C and D. The purple, dark blue and light blue are constraints contours at 68, 95 and 99% confidence limit in the case of our baseline fit (F1, without X-ray imaging prior on the gas density). For sub-cluster B, the red contours are similar to the blue ones in the case of the fit F2 (with the X-ray imaging prior). The marginalized probability density distribution are also given by the histograms in the case of F1. The dashed line give the zero location of the velocity axis.

6.5. Comparison to previous results

The raw NIKA and Bolocam maps can hardly be compared directly, because they probe different angular scales due to beam smoothing and large scale filtering. However, the best fit model of Sayers et al. (2013) and our best fit model are deconvolved from the respective transfer functions and they can quantitatively be compared. Nevertheless, while we consider a physical parametric description of the ICM, Sayers et al. (2013) use X-ray data to predict a tSZ template, to which they add a β -model component to include the kSZ signal. Each model has its pros and cons and both are clearly limited in the case of a complex system as MACS J0717.5+3745. Our model is clearly a strong idealization of the cluster, but it allows for a self-consistent description of the ICM. The model of Sayers et al. (2013), on the other hand, does not assume any parametrization of the ICM for the tSZ signal, but it does use a β -model for the kSZ, and the two are not necessarily related to the same underlying gas density distribution. The tSZ template build by Sayers et al. (2013) is based on X-ray data and is therefore likely to reproduce better the projected geometry of the cluster than our model. However, it requires to convert $\int n_e^2 dl$, which is the quantity to which X-ray are sensitive, to $\int n_e dl$ as needed for the tSZ template. This is done via an effective line of sight extent of the ICM, left as a free parameter, but taken as a constant for the entire cluster. This is a strong assumption and our baseline model is not sensitive to such effect. Sayers et al. (2013) assume that the temperature is constant along the line of sight, while we assume isothermal clumps, both being based on X-ray spectroscopy. Finally, Sayers et al. (2013) use fixed coordinates for their β -model center and check a posteriori the effect of changing them within reasonable uncertainties. Due to the higher angular resolution of NIKA, we fully marginalize over the clump coordinates in our fit.

Table 7 summarizes velocity measurements performed towards MACS J0717.5+3745. Despite the fact that the cluster is modeled differently, our constraints on the gas line of sight velocity are overall compatible with the results from Sayers et al. (2013). In the case of sub-cluster C, however, the two results are in mild tension ($\gtrsim 2\sigma$). While this could easily be attributed to mis-modeling, it could also be due to differences in the observations. Indeed, our data are sensitive to scales as low as ~ 20 arcsec, and the constraint in region C is driven by the positive peak seen at 260 GHz at small scales. Due to Bolocam larger beams, the corresponding scales are likely to

be diluted over the cluster regions, leading to velocity averaged over a larger extent and hence smaller. Such effect are also likely affecting region B, but they might be less important because sub-cluster B is more isolated. In addition to the velocity, we can also use our model to infer the integrated Compton parameter in the regions considered by Sayers et al. (2013). We compute $Y(\Omega) = \int y_{\text{tSZ}} d\Omega$, where Ω is taken as a circular region of 60 arcsec diameter centered on sub-clusters B and C, using the same center coordinates as Sayers et al. (2013). We obtain $(0.173 \pm 0.024) \times 10^{-3}$ arcmin 2 for region B ($(0.221 \pm 0.015) \times 10^{-3}$ arcmin 2 in the case of X-ray prior on the density), and $(0.242 \pm 0.024) \times 10^{-3}$ arcmin 2 for region C. These values are in agreement within 1σ (2σ in the case of X-ray prior on the density) of the values provided by Sayers et al. (2013).

Our constraints are also roughly compatible with the optical spectroscopic measurement of Ma et al. (2009) within error bars. However, as discussed in section 5.5, our data hint for sub-structure within sub-clusters B and C themselves. As a possible consequence, our measurement in the direction of sub-cluster C, which is dominated by the half north part of the region, indicates higher velocities than what is measured in optical. Additional optical spectroscopy, in order to obtain more galaxy redshifts, would be necessary to better address the comparison between the galaxy velocities and the gas velocity.

Finally, Ruan et al. (2013) have computed the tSZ and kSZ maps along different projection of a strongly interacting cluster similar to MACS J0717.5+3745, in particular in terms of velocity distribution. Therefore, we compare qualitatively this simulation to our observations. Our tSZ and kSZ maps compare very well to the simulated cluster. The signal we observe matches their simulation both in term of amplitude and of structure of the signal, with peaked kSZ emission reaching $\sim 2 \times 10^{-4}$ in units of y_{kSZ} , in their simulation. The tSZ signal, on the other hand, is more diffuse. This qualitative agreement between our data and the simulation of Ruan et al. (2013) confirms that MACS J0717.5+3745 is an exceptionally disturbed system.

The root mean square of cluster peculiar velocities is expected to be of the order of 250 km/s (e.g., Hernández-Monteagudo & Sunyaev 2010). Therefore, the velocities we measure in MACS J0717.5+3745 deviate significantly from the bulk velocity flow. However, the free fall of massive sub-clusters onto one another from large distances is expected to lead to relative velocities of several thousands of km/s (Sarazin 2002). The velocities measured in MACS J0717.5+3745 are therefore quite

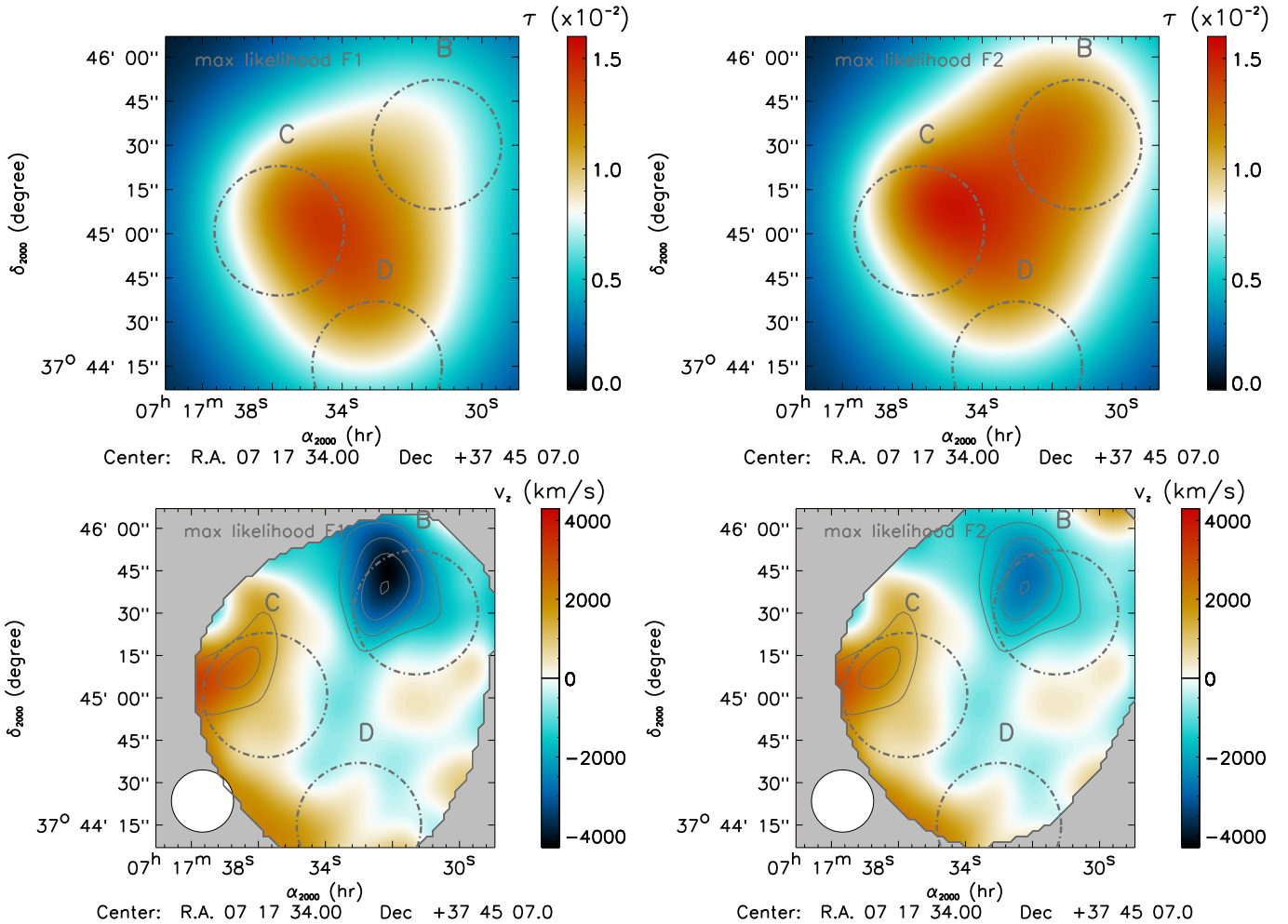


Figure 9. **Top:** map of the best fit optical depth model. **Bottom:** projected gas line of sight velocity map reconstructed toward MACS J0717.5+3745. The left panel correspond to fit F1 and the right panel to fit F2. Regions where the root mean squared of the noise is larger than 3 times the minimum value have been masked for display purpose. Contours are spaced by 1σ , starting at $\pm 2\sigma$. Note that the field shown in here is smaller than the other ones displayed in this paper.

high, but in line with expectations. Moreover, our results suggest that many other well known mergers could be ideal targets to explore their kinematics from kSZ mapping.

7. Summary and conclusions

The triple merging cluster of galaxy, MACS J0717.5+3745, was observed using the NIKA camera at the IRAM 30m telescope. The cluster SZ diffuse emission is detected in the two NIKA bands, 150 and 260 GHz. We also report the detection of radio and sub-millimeter point sources that contaminates our data. Using radio data from the literature and sub millimeter data from SPIRE, in addition to the NIKA constraints themselves, we model the contaminant sources and extrapolate them to the NIKA bands to clean our data. We note that one of the sub-millimeter source detected with NIKA coincide with a high redshift lensed galaxy detected by HST, in agreement with its SED which peak at about 500 μm . If confirmed, this would illustrate the possibility of finding high redshift sources lensed by clusters of galaxies by combining NIKA to Herschel data. In addition to the point source removal, we take advantage of the high resolution of the NIKA observations to mask possible residuals.

The noise contained in our data includes uncorrelated instrumental noise, atmospheric and electronic correlated noise resid-

uals and a significant contribution from the CIB, which we take into account. While the non astrophysical noise reduces by increasing the integration time, this is not the case for the CIB. Since our kSZ mapping is limited by statistics, itself dominated by the noise in our 260 GHz band, the CIB is already non negligible for the data we present, for a projected integration time of 13.1 hours on target. Therefore, this work shows that the CIB is likely to be a limiting factor for future high angular resolution kSZ mapping at these frequencies.

By combining the two NIKA bands, under the assumption that the SZ signal is the sum of a tSZ and a kSZ contribution, we extract the first map of the kSZ effect toward a cluster of galaxy. We account for relativistic corrections from X-ray spectroscopic data, which we use to produce a temperature map. The kSZ map is dominated by a dipolar structure with peak emission in the direction of region B (negative) and C (positive). This is in agreement with the merger scenario in which sub-cluster B is a compact core falling onto the main cluster and C being the most massive sub-cluster, undergoing a violent merger with sub-cluster D. However, our data indicates that sub-cluster B and C are themselves likely to be made of sub-components. Our results complement that of Sayers et al. (2013) at different scales. Apart from the relativistic corrections, which assume a constant tem-

Table 7. Comparison of the constraints of the velocity of sub-clusters in MACS J0717.5+3745. The NIKA results do not include calibration uncertainties or errors in the X-ray temperature of each clumps.

Sub-cluster	Galaxies Optical (Ma et al. 2009)	v_z (km/s) Gas (kSZ) (Sayers et al. 2013)	Gas (kSZ) NIKA (F1)	Gas (kSZ) NIKA (F2)
A	278^{+295}_{-339}	—	—	—
B	3238^{+252}_{-242}	3450 ± 900	66^{+2312}_{-109} 	2058^{+486}_{-447}
C	-733^{+486}_{-478}	-550^{+1350}_{-1400}	-4^{+394}_{-104}	—
D	831^{+843}_{-800}	—	150^{+1510}_{-1208}	—

perature along the line of sight, the kSZ map we present in this paper is model independent.

We use the NIKA surface brightness maps in addition to X-ray temperature estimates of each sub-clusters to constrain the gas density and velocity distribution in MACS J0717.5+3745. The gas density model assumes that each sub-cluster is described by a β -model with constant line of sight velocity and temperature. We perform a MCMC fit and provide constraints on the gas velocity toward each sub-cluster. While sub-cluster D is consistent with null line of sight velocity, it is not the case for sub-cluster B and C which are moving away from us and toward us in the CMB reference frame, respectively. The relative significance of our measurement is stable and model independent, but the absolute velocity depends on our assumptions in the structure of the gas of MACS J0717.5+3745. Our constraints are limited by degeneracies between the sub-clusters optical depth and their velocity, and by the simplicity of our model, which is a strong idealization for a system known to be one of the most complex cluster of galaxies. Despite this limitation, our results allow us to study in detail the gas motion in the cluster and complement other observations of MACS J0717.5+3745.

The results presented in this paper open a new way to study the distribution of the gas velocity within galaxy clusters, which is essential to understand the dynamics of mergers at the sub-structure level.

Acknowledgements. We are grateful to Jack Sayers for helping us obtaining the Herschel SPIRE catalog we use in this paper. We would like to thank the IRAM staff for their support during the campaigns. The NIKA dilution cryostat has been designed and built at the Institut Néel. In particular, we acknowledge the crucial contribution of the Cryogenics Group, and in particular Gregory Garde, Henri Rodenas, Jean Paul Leggeri, Philippe Camus. This work has been partially funded by the Foundation Nanoscience Grenoble, the LabEx FOCUS ANR-11-LABX-0013 and the ANR under the contracts "MKIDS", "NIKA" and ANR-15-CE31-0017. This work has benefited from the support of the European Research Council Advanced Grant ORISTARS under the European Union's Seventh Framework Programme (Grant Agreement no. 291294). We acknowledge fundings from the ENIGMASS French LabEx (B. C. and F. R.), the CNES post-doctoral fellowship program (R. A.), the CNES doctoral fellowship program (A. R.) and the FOCUS French LabEx doctoral fellowship program (A. R.). E.P. acknowledges the support of the French Agence Nationale de la Recherche under grant ANR-11-BD56-015.

References

- Adam, R. et al. 2016, A&A, 586, A122, 1510.06674
 —. 2015, A&A, 576, A12, 1410.2808
 —. 2014, A&A, 569, A66, 1310.6237
 Allen, S. W., Evrard, A. E., & Mantz, A. B. 2011, ARA&A, 49, 409, 1103.4829
 Atrio-Barandela, F. 2013, A&A, 557, A116, 1303.6614
 Bartalucci, I., Mazzotta, P., Bourdin, H., & Vikhlinin, A. 2014, A&A, 566, A25, 1404.3587
 Becker, R. H., White, R. L., & Helfand, D. J. 1995, ApJ, 450, 559
 Benson, B. A. et al. 2003, ApJ, 592, 674, astro-ph/0303510
 Béthermin, M. et al. 2012, ApJ, 757, L23, 1208.6512
 Béthermin, M., Wang, L., Doré, O., Lagache, G., Sargent, M., Daddi, E., Cousin, M., & Aussel, H. 2013, A&A, 557, A66, 1304.3936
 Bhattacharya, S., & Kosowsky, A. 2007, ApJ, 659, L83, astro-ph/0612555
 —. 2008, Phys. Rev. D, 77, 083004, 0712.0034
 Birkinshaw, M. 1999, Phys. Rep., 310, 97, arXiv:astro-ph/9808050
 Bleem, L. E. et al. 2015, ApJS, 216, 27, 1409.0850
 Bonafede, A. et al. 2009, A&A, 503, 707, 0905.3552
 Bourdin, H., & Mazzotta, P. 2008, A&A, 479, 307, 0802.1866
 Bourdin, H., Mazzotta, P., Markevitch, M., Giacintucci, S., & Brunetti, G. 2013, ApJ, 764, 82, 1302.0696
 Bourdin, H., Sauvageot, J.-L., Slezak, E., Bijaoui, A., & Teyssier, R. 2004, A&A, 414, 429
 Calvo, M. et al. 2013, A&A, 551, L12
 Carlstrom, J. E., Holder, G. P., & Reese, E. D. 2002, ARA&A, 40, 643, arXiv:astro-ph/0208192
 Catalano, A. et al. 2014, A&A, 569, A9, 1402.0260
 Cavaliere, A., & Fusco-Femiano, R. 1978, A&A, 70, 677
 Chib, S., & Greenberg, E. 1995, The American Statistician, 49, 327
 Clowe, D., Bradač, M., Gonzalez, A. H., Markevitch, M., Randall, S. W., Jones, C., & Zaritsky, D. 2006, ApJ, 648, L109, astro-ph/0608407
 Coble, K. et al. 2007, AJ, 134, 897, astro-ph/0608274
 Colafrancesco, S. 2004, A&A, 422, L23, astro-ph/0405456
 —. 2008, MNRAS, 385, 2041, 0801.4535
 Condon, J. J., Cotton, W. D., Greisen, E. W., Yin, Q. F., Perley, R. A., Taylor, G. B., & Broderick, J. J. 1998, AJ, 115, 1693
 Coppin, K. E. K. et al. 2011, MNRAS, 416, 680, 1105.3199
 Diego, J. M., Broadhurst, T., Zitrin, A., Lam, D., Lim, J., Ford, H. C., & Zheng, W. 2015, MNRAS, 451, 3920, 1410.7019
 Ebeling, H., Barrett, E., & Donovan, D. 2004, ApJ, 609, L49, astro-ph/0406049
 Ebeling, H., Barrett, E., Donovan, D., Ma, C.-J., Edge, A. C., & van Speybroeck, L. 2007, ApJ, 661, L33, astro-ph/0703394
 Ebeling, H., Edge, A. C., & Henry, J. P. 2001, ApJ, 553, 668, astro-ph/0009101
 Edge, A. C., Ebeling, H., Bremer, M., Röttgering, H., van Haarlem, M. P., Rengelink, R., & Courtney, N. J. D. 2003, MNRAS, 339, 913
 Ferrari, C., Benoist, C., Maurogordato, S., Cappi, A., & Slezak, E. 2005, A&A, 430, 19, astro-ph/0409072
 Fixsen, D. J. 2009, ApJ, 707, 916, 0911.1955
 Freeman, P. E., Kashyap, V., Rosner, R., & Lamb, D. Q. 2002, ApJS, 138, 185, astro-ph/0108429
 Garmire, G. P., Bautz, M. W., Ford, P. G., Nousek, J. A., & Ricker, Jr., G. R. 2003, in Proc. SPIE, Vol. 4851, X-Ray and Gamma-Ray Telescopes and Instruments for Astronomy., ed. J. E. Truemper & H. D. Tananbaum, 28–44
 Gelman, A., & Rubin, D. B. 1992, Statistical Science, 7, 457
 Greve, A., Neri, R., & Sievers, A. 1998, A&AS, 132, 413
 Griffin, M. J. et al. 2010, A&A, 518, L3, 1005.5123
 Haehnelt, M. G., & Tegmark, M. 1996, MNRAS, 279, 545, astro-ph/9507077
 Hahn, O., Angulo, R. E., & Abel, T. 2015, MNRAS, 454, 3920, 1404.2280
 Hall, N. R. et al. 2010, ApJ, 718, 632, 0912.4315
 Hand, N. et al. 2012, Physical Review Letters, 109, 041101, 1203.4219
 Hasselfield, M. et al. 2013, J. Cosmology Astropart. Phys., 7, 008, 1301.0816
 Hernández-Monteagudo, C., & Sunyaev, R. A. 2010, A&A, 509, A82, 0905.3001
 Hernández-Monteagudo, C., Verde, L., Jimenez, R., & Spergel, D. N. 2006, ApJ, 643, 598, astro-ph/0511061
 Holzapfel, W. L., Ade, P. A. R., Church, S. E., Mauskopf, P. D., Rephaeli, Y., Wilbanks, T. M., & Lange, A. E. 1997, ApJ, 481, 35, astro-ph/9702223
 Itoh, N., & Nozawa, S. 2003, ArXiv Astrophysics e-prints, astro-ph/0307519
 Jauzac, M. et al. 2012, MNRAS, 426, 3369, 1208.4323
 Johnson, T. L., Sharon, K., Bayliss, M. B., Gladders, M. D., Coe, D., & Ebeling, H. 2014, ApJ, 797, 48, 1405.0222
 Kalberla, P. M. W., Burton, W. B., Hartmann, D., Arnal, E. M., Bajaja, E., Morras, R., & Pöppel, W. G. L. 2005, A&A, 440, 775, astro-ph/0504140
 Kartaltepe, J. S., Ebeling, H., Ma, C. J., & Donovan, D. 2008, MNRAS, 389, 1240, 0806.4019

- Kashlinsky, A., Atrio-Barandela, F., Kocevski, D., & Ebeling, H. 2008, ApJ, 686, L49, 0809.3734
- Kawamata, R., Oguri, M., Ishigaki, M., Shimasaku, K., & Ouchi, M. 2015, ArXiv e-prints, 1510.06400
- Kitayama, T. 2014, Progress of Theoretical and Experimental Physics, 2014, 060000, 1404.0870
- Kosowsky, A., & Bhattacharya, S. 2009, Phys. Rev. D, 80, 062003, 0907.4202
- Kravtsov, A. V., & Borgani, S. 2012, ARA&A, 50, 353, 1205.5556
- Kuntz, K. D., & Snowden, S. L. 2000, ApJ, 543, 195
- LaRoque, S. J. et al. 2003, ApJ, 583, 559
- Limousin, M. et al. 2012, A&A, 544, A71, 1109.3301
—. 2015, ArXiv e-prints, 1510.08077
- Lumb, D. H., Warwick, R. S., Page, M., & De Luca, A. 2002, A&A, 389, 93, astro-ph/0204147
- Ma, C.-J., Ebeling, H., & Barrett, E. 2009, ApJ, 693, L56, 0901.4783
- Ma, Y.-Z., & Zhao, G.-B. 2014, Physics Letters B, 735, 402, 1309.1163
- Martino, R., Mazzotta, P., Bourdin, H., Smith, G. P., Bartalucci, I., Marrone, D. P., Finoguenov, A., & Okabe, N. 2014, MNRAS, 443, 2342, 1406.6831
- Maurogordato, S., Sauvageot, J. L., Bourdin, H., Cappi, A., Benoist, C., Ferrari, C., Mars, G., & Houairi, K. 2011, A&A, 525, A79, 1009.1967
- Medezinski, E. et al. 2013, ApJ, 777, 43, 1304.1223
- Monfardini, A. et al. 2011, ApJS, 194, 24, 1102.0870
- Mroczkowski, T. et al. 2012, ApJ, 761, 47, 1205.0052
- Nozawa, S., Itoh, N., Suda, Y., & Ohhata, Y. 2006, Nuovo Cimento B Serie, 121, 487, astro-ph/0507466
- Pandey-Pommier, M., Richard, J., Combes, F., Dwarakanath, K. S., Guiderdoni, B., Ferrari, C., Sirothia, S., & Narasimha, D. 2013, A&A, 557, A117
- Pardo, J., Cernicharo, J., & Serabyn, E. 2002, in Astronomical Society of the Pacific Conference Series, Vol. 266, Astronomical Site Evaluation in the Visible and Radio Range, ed. J. Vernin, Z. Benkhaldoun, & C. Muñoz-Tuñón, 188
- Planck Collaboration et al. 2016, ArXiv e-prints, 1603.04919
—. 2014a, A&A, 571, A30, 1309.0382
—. 2015a, ArXiv e-prints, 1504.03339
—. 2014b, A&A, 561, A97, 1303.5090
—. 2015b, ArXiv e-prints, 1502.01589
—. 2015c, ArXiv e-prints, 1502.01597
- Ponthieu, N., Grain, J., & Lagache, G. 2011, A&A, 535, A90, 1111.0766
- Postman, M. et al. 2012, ApJS, 199, 25, 1106.3328
- Pratt, G. W., Böhringer, H., Croston, J. H., Arnaud, M., Borgani, S., Finoguenov, A., & Temple, R. F. 2007, A&A, 461, 71, astro-ph/0609480
- Ruan, J. J., Quinn, T. R., & Babul, A. 2013, MNRAS, 432, 3508, 1304.6088
- Sarazin, C. L. 2002, in Astrophysics and Space Science Library, Vol. 272, Merging Processes in Galaxy Clusters, ed. L. Feretti, I. M. Gioia, & G. Giovannini, 1–38, astro-ph/0105418
- Sayers, J. et al. 2013, ApJ, 778, 52, 1312.3680
—. 2015, ArXiv e-prints, 1509.02950
- Schellenberger, G., Reiprich, T. H., Lovisari, L., Nevalainen, J., & David, L. 2015, A&A, 575, A30, 1404.7130
- Scheuer, P. A. G., & Williams, P. J. S. 1968, ARA&A, 6, 321
- Smith, R. K., Brickhouse, N. S., Liedahl, D. A., & Raymond, J. C. 2001, ApJ, 556, L91, astro-ph/0106478
- Snowden, S. L., Collier, M. R., & Kuntz, K. D. 2004, The Astrophysical Journal, 610, 1182
- Soergel, B. et al. 2016, ArXiv e-prints, 1603.03904
- Strüder, L. et al. 2001, A&A, 365, L18
- Sunyaev, R. A., & Zeldovich, I. B. 1980, MNRAS, 190, 413
- Sunyaev, R. A., & Zeldovich, Y. B. 1972, Comments on Astrophysics and Space Physics, 4, 173
- Tucci, M., Toffolatti, L., de Zotti, G., & Martínez-González, E. 2011, A&A, 533, A57, 1103.5707
- Tully, R. B., & Fisher, J. R. 1977, A&A, 54, 661
- Turner, M. J. L. et al. 2001, A&A, 365, L27, astro-ph/0011498
- van Weeren, R. J., Röttgering, H. J. A., Brüggen, M., & Cohen, A. 2009, A&A, 505, 991, 0905.3650
- Voit, G. M. 2005, Reviews of Modern Physics, 77, 207, astro-ph/0410173
- Wang, Q., Markevitch, M., & Giacintucci, S. 2016, ArXiv e-prints, 1603.05232
- Zemcov, M. et al. 2013, ApJ, 769, L31, 1303.6725
- Zitrin, A., Broadhurst, T., Barkana, R., Rephaeli, Y., & Benítez, N. 2011, MNRAS, 410, 1939, 1002.0521
- Zitrin, A., Broadhurst, T., Rephaeli, Y., & Sadeh, S. 2009, ApJ, 707, L102, 0907.4232
- Zitrin, A. et al. 2015, ApJ, 801, 44, 1411.1414